SUPPLEMENTARY INFORMATION

Heterointerface promoted trifunctional electrocatalysts for all temperature high-performance rechargeable Zn-air batteries

Nayantara K. Wagh[1#], Dong-Hyung Kim[1#], Chi Ho Lee[2], Sung-Hae Kim[1], Han-Don Um[3], Joseph Sang-Il Kwon[2], Sambhaji S. Shinde[1*], Sang Uck Lee[4], Jung-Ho Lee[1*]

[1]Department of Materials Science and Chemical Engineering, Hanyang University, Ansan, Republic of Korea

[2]Artie McFerrin Department of Chemical Engineering, Texas A&M University, College Station, Texas 77843, United States; Texas A&M Energy Institute, College Station, Texas 77843, United States.

[3]Department of Chemical Engineering, Kangwon National University, Chuncheon, Gangwon-do 24341, Republic of Korea.

[4]School of Chemical Engineering, Sungkyunkwan University, 2066 Seobu-ro, Jangan-gu, Suwon, Gyeonggi-do 16419, Republic of Korea.

List of Contents

1. Supplementary experimental methods

Catalyst fabrication

Chemicals: Cobalt (II) chloride dehydrate ($CoCl_2.2H_2O$), Tin (II) chloride dihydrate ($SnCl_2.2H_2O$), Sodium sulfide (Na_2S), Graphite powder, poly(N-vinyl-2-pyrrolidone) (M_W = 40,000), Chloroplatinic acid ($H_2PtCl_6 \cdot 6H_2O$), Potassium permanganate ($KMnO_4$), and Nafion were obtained with the Sigma-Aldrich. N,N-Dimethylformamide (C_3H_7ON), ethanol (C_2H_5OH), acetone, sodium hydroxide (NaOH), potassium hydroxide (KOH), sulfuric acid (H_2SO_4), zinc acetate ($Zn(OAc)_2$), and nitric acid (HNO_3) were attained from Daejung Chemicals. Carbon paper and stainless steel mesh (Spectra carb 2040-A, Fuel Cell Store), and Zn plate (Sigma-Aldrich, USA) were used as received. All precursors were used without further purifications. Deionized water was utilized as solvent until otherwise specifically mentioned. Acquired resources were applied further without distillation.

Synthesis of reference Pt/C catalysts

$H_2PtCl_6 \cdot 6H_2O$ was reacted with an appropriate amount of poly(N-vinyl-2-pyrrolidone) (M_W = 40,000) solution under vigorous stirring, followed by the addition of activated carbon. After that, the sodium borohydride ($NaBH_4$) solution was appended to the reaction mixture under stirring for 30 min. Finally, the obtained mixture was collected after centrifugation, several times cleanings with deionized water, and dried at 60 °C for 12 h.

Synthesis of the RuO_2 catalysts

The 50 mM ruthenium (III) chloride hydrate was dispersed in the mixture of deionized water and methyl alcohol (1:1 v/v) under continuous rotations. Further, the 2 M NaOH was injected drop-by-drop into the above reaction mixture until the pH of the solution became 7. The obtained product was centrifuged, rinsed with deionized water, and dehydrated at 60 °C, followed by annealing at 500 °C for 5 h in air.

Characterization of the prepared catalysts

Powder X-ray diffraction (PXRD) patterns were measured on Rigaku Smartlab D/max 2500Pc diffractometer with Cu Kα radiation (wavelength of 1.5406 Å). Morphology images were performed by field-emission scanning electron microscopy (FESEM, JEOL-6700F). Transmission electron microscopy (TEM) images were acquired on a Cs-corrected Titan™ 80-300 with an accelerating voltage of 80 kV. Elemental composition maps were recorded by

an EDS attached to the TEM. Raman spectra were measured on a RM 1000 (Ranishaw, UK) spectrometer. X-ray photoelectron spectroscopy (XPS) was performed on a VG SCIENTA (R 3000) spectrometer equipped with a monochromatic Al *K*α source.

Electrochemical measurements

The electrochemical performances were performed on an electrochemical workstation (CHI 760 D, CH Instruments) at room temperature with a typical three-electrode electrochemical cell. The Ag/AgCl (with saturated KCl) reference electrode, a graphite rod as the counter electrode, a glassy carbon (GC) rotating disk electrode (RDE, 0.196 cm^2) coated with the catalysts as the working electrode, and 0.1 M aqueous KOH (oxygen-rich) as the electrolyte. The working electrode was fabricated with as-obtained $SnS_{2-\delta}$ or $CoS_{1-\delta}$ or $CoS_{1-\delta}/SnS_{2-\delta}$ catalysts placed over the GC using Nafion adhesive (5 wt%, 2 μl) and then dried at room temperature for several hours. For comparison, Pt/C and RuO_2 reference materials inks were prepared by dispersing 10 mg of catalysts in the propanol of 1.95 ml and Nafion of 50 μl. Then, 4 μL of the prepared inks were evenly loaded on the GC surface and dried at room temperature. Mass loading for both fabricated catalysts was fixed to be 0.10 mg cm^{-2} for both oxygen reactions. Prior to the ORR/OER measurements, the electrolyte (0.1 M KOH) was saturated by oxygen, and nitrogen flow for 30 min. LSV profiles for ORR/OER were obtained for 1600 rpm with a scan rate of 5 mV s^{-1} in the potential range of 0.2–2 V vs. RHE. Chronoamperometric half-cell reactions durability was evaluated at the respective overpotentials for OER and half-wave potential for ORR. The measured potentials were referenced to the reversible hydrogen electrode (RHE) according to the Nernst equation,

$$E_{RHE} = E_{Ag/Ag/Cl} + 0.059 \times pH + 0.205 \quad \text{(S1)}$$

Performed current densities were also referenced according to the measured geometric surface areas. Electrochemical impedance spectra were obtained for the frequency range of 100 Hz to 1 MHz with a constant bias of 0.2 V. The long-life durability of the catalysts was measured by continuous potentiodynamic sweeps for a scan rate of 100 mV s^{-1}. Mass loading of $CoS_{1-\delta}/SnS_{2-\delta}$ catalysts, reference Pt/C, and RuO_2 has been placed similarly unless otherwise stated (0.1 mg cm^{-2}).

Oxygen reduction reaction kinetics

The ORR kinetics were evaluated by using different rotational speed LSV profiles. The measured total current density is the sum of the inverse of kinetic current (J_K) and diffusion

current (J_d). Every atom or ion on the electrode reacts immediately as the applied overpotential is sufficiently high. The number of oxygen molecules at the electrode surface is almost zero, facilitating a diffusion-limiting plateau. Therefore, the diffusion current is related only to the RDE rotational speeds.

The transferred electron number (n) in oxygen reduction was determined according to the Koutecky–Levich (K–L) equation[S1-S3]:

$$\frac{1}{J} = \frac{1}{J_K} + \frac{1}{B\omega^{1/2}} \quad \text{(S2)}$$

$$B = 0.2nF(D_{O_2})^{2/3}\nu^{-1/6}C_{O_2} \quad \text{(S3)}$$

where B represents the Levich slope, J_K represents the kinetic current, J represents the measured total current, ω represents the electrode rotation rate, n represents the number of electrons transferred for each oxygen molecule, F represents the Faraday constant (F = 96485 C mol^{-1}), D_{O2} represents the O_2 diffusion coefficient in 0.1 M KOH (D_{O2} = 1.9 × 10^{-5} cm^2 s^{-1}), ν represents the kinetic viscosity (0.01 cm^2 s^{-1}) and C_{O2} represents the concentration of O_2 (C_{O2} = 1.2 × 10^{-6} mol cm^{-3}). The considered rotation speeds are in rpm, and therefore, the constant factor 0.2 is multiplied. The peroxide species during ORR reactions were determined by measuring the RRDE polarization profiles for the ring potential of 1.3 V *vs.* RHE. Based on the following expressions, the transferred electron number (n) and peroxide (H_2O_2) yield were evaluated as[S4]:

$$n = 4\frac{I_d}{I_d + I_r/N} \quad \text{(S4)}$$

and

$$H_2O^-(\%) = 100\frac{2I_r/N}{I_d + I_r/N} \quad \text{(S5)}$$

where I_r represents the ring current, I_d represents the disk current, and N represents the current collection efficiency of the Pt ring. N was determined to be 0.42.

Fabrication of Zn-air batteries (ZABs)

Alkaline Zn–air batteries

The alkaline rechargeable ZABs were analyzed using the home-constructed electrochemical cells. Air cathodes were constructed by uniform mixing of $CoS_{1-\delta}/SnS_{2-\delta}$ catalysts, carbon black, and polytetrafluoroethylene binder (8:1:1) and carbon paper was utilized as current collectors. Further, for comparison, Pt/C + RuO_2 catalyst slurry was fabricated by mixing

carbon black, polytetrafluoroethylene, and the catalysts (1:1:8 w/w) in ethanol/Nafion solution. The mass loadings of the $CoS_{1-\delta}/SnS_{2-\delta}$ and reference Pt/C+RuO_2 catalysts for alkaline ZABs was 1 mg cm^{-2}. The mass ratio of reference Pt/C and RuO_2 was 1:1. Here, 6 M KOH with 0.2 M zinc acetate was used as the liquid electrolyte for the reversible electrochemical reactions. Catalyst-loaded (Pt/C+RuO_2) carbon paper was used as an air cathode and a polished Zn plate (0.5 mm thickness) as anode.

Flexible solid-state Zn–air batteries

Flexible ZABs were assembled with $CoS_{1-\delta}/SnS_{2-\delta}$ catalysts coated stainless steel mesh as the air cathodes (8:1:1 composition for catalysts, carbon black and polytetrafluoroethylene binder), the chitosan biocellulosics (CBCs fabricated as per our previous reference[1]) as the solid electrolyte (70 μm), and Zn foil (0.3 mm) as the anode. Then, $CoS_{1-\delta}/SnS_{2-\delta}$ based catalysts and zinc foils were situated on the opposite sides of the CBCs electrolyte. Finally, the fabricated devices were pressed cautiously and encapsulated with sustainable latex. For comparison, Pt/C + RuO_2 catalyst slurry was also fabricated by mixing carbon black, polytetrafluoroethylene, and the catalysts (1:1:8 w/w) in ethanol/Nafion solution. The mass loadings of the $CoS_{1-\delta}/SnS_{2-\delta}$ and reference Pt/C+RuO_2 catalysts for rechargeable ZABs was 2 mg cm^{-2} and electrode area of 2 cm^2.

Battery testing

Note all the measurements were carried out in ambient conditions. The galvanostatic discharge and charge voltage profiles were conducted on a WONATEC multichannel battery testing system. The cycling for alkaline and flexible solid ZABs was performed for 10 min per cycle (charge: 5 min; discharge: 5 min) for current densities of 10 and 25 mA cm^{-2}, respectively. The specific capacities were determined using the galvanostatic discharge profiles standardized to the utilized mass of Zn. The energy efficiency was calculated from the ratio of discharge to charge voltages. The power densities of both ZABs were calculated by expression as $P = V \times I$.

Supplementary Figures

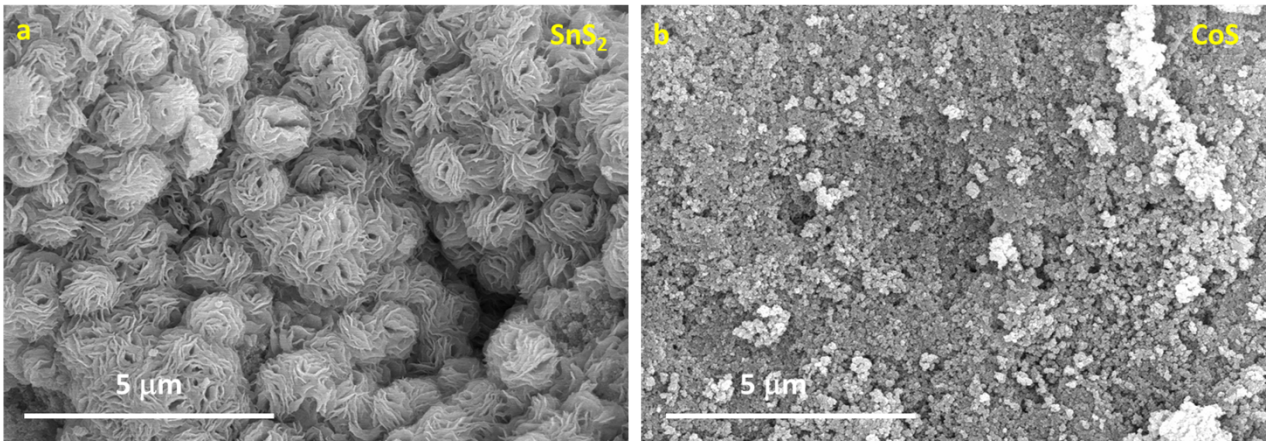

Figure S1. Microscopic characterizations. SEM images for fabricated pristine SnS_2 and CoS catalysts.

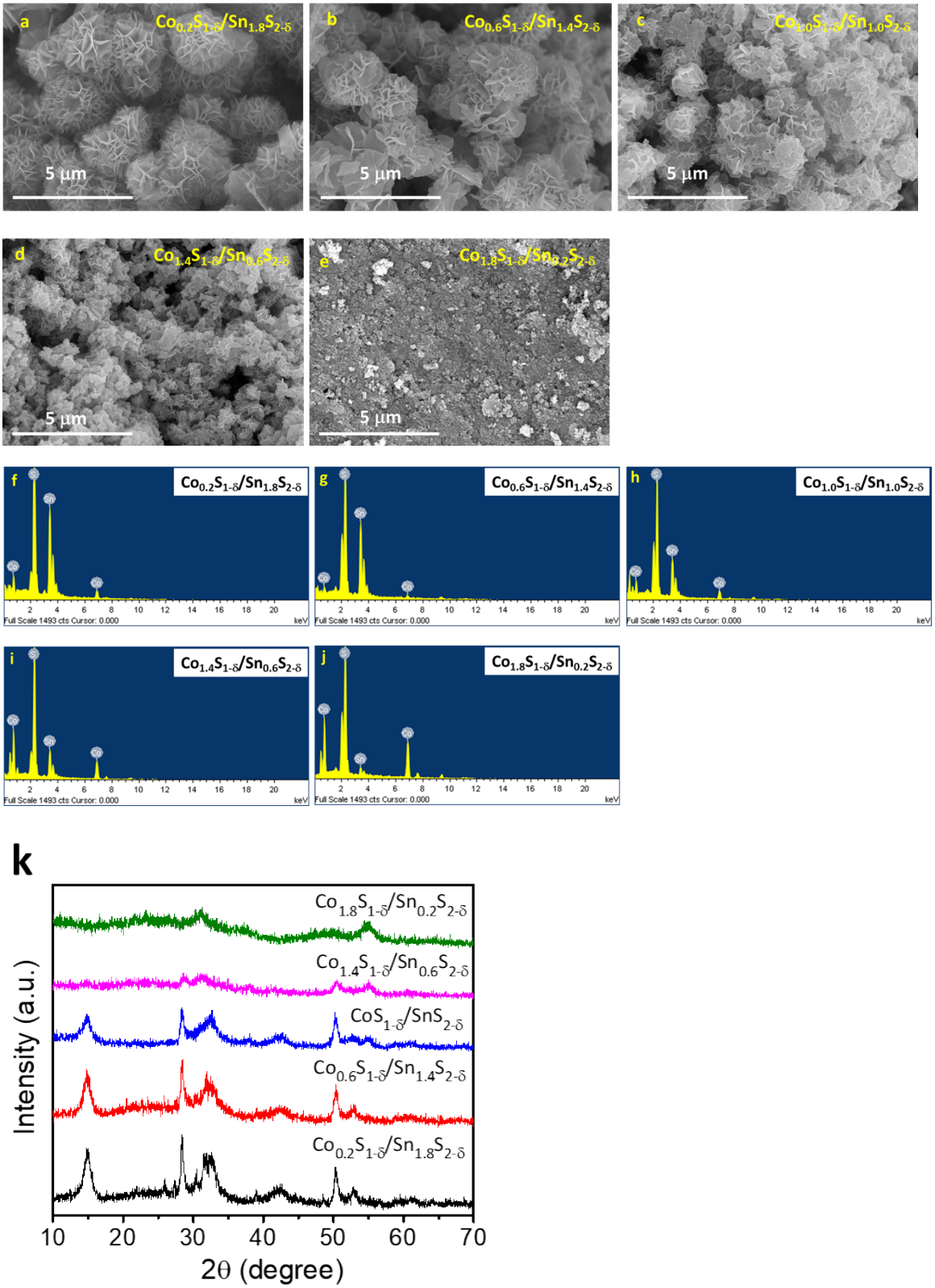

Figure S2. Microscopic characterizations. (a-e) SEM images, (f-j) EDS spectra, and (k) XRD patterns for fabricated $Co_{0.2}S_{1-\delta}/Sn_{1.8}S_{2-\delta}$, $Co_{0.6}S_{1-\delta}/Sn_{1.4}S_{2-\delta}$, $Co_{1.0}S_{1-\delta}/Sn_{1.0}S_{2-\delta}$, $Co_{1.4}S_{1-\delta}/Sn_{0.6}S_{2-\delta}$, and $Co_{1.8}S_{1-\delta}/Sn_{0.2}S_{2-\delta}$ hetero-interface based catalysts with varying composition from 0.2 to 1.8 for Co and Sn, respectively.

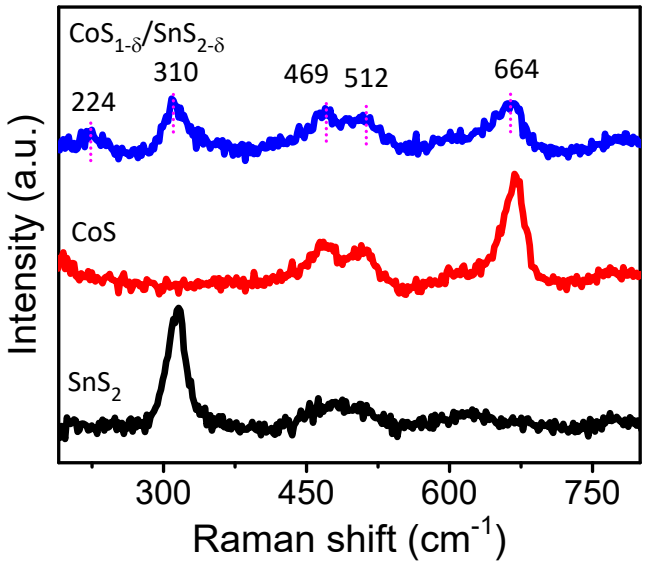

Figure S3. Spectroscopic characterization. Raman spectra for SnS_2, CoS, and $CoS_{1-\delta}/SnS_{2-\delta}$ catalysts.

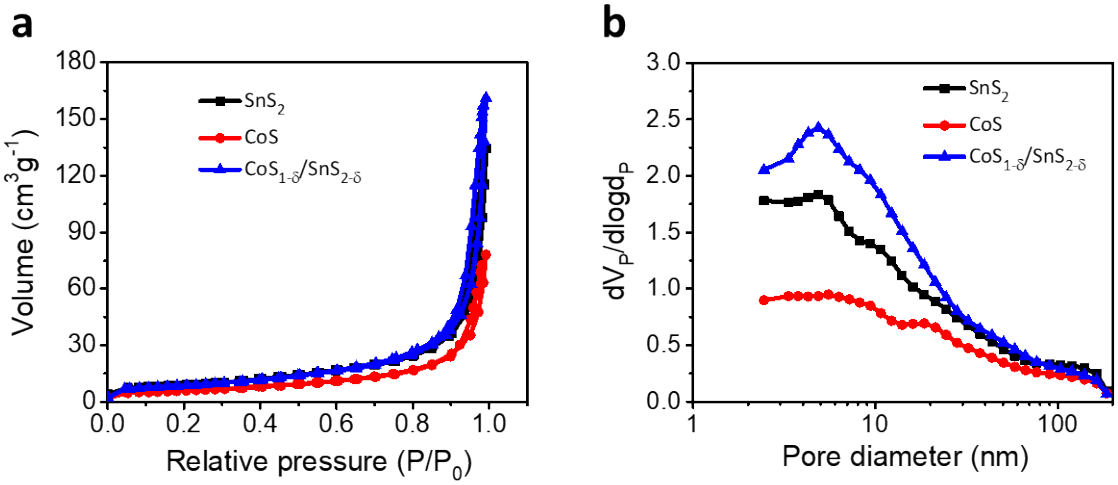

Figure S4. BET characterization. (a) Nitrogen sorptions and (b) pore distributions for SnS_2, CoS, and $CoS_{1-\delta}/SnS_{2-\delta}$ catalysts.

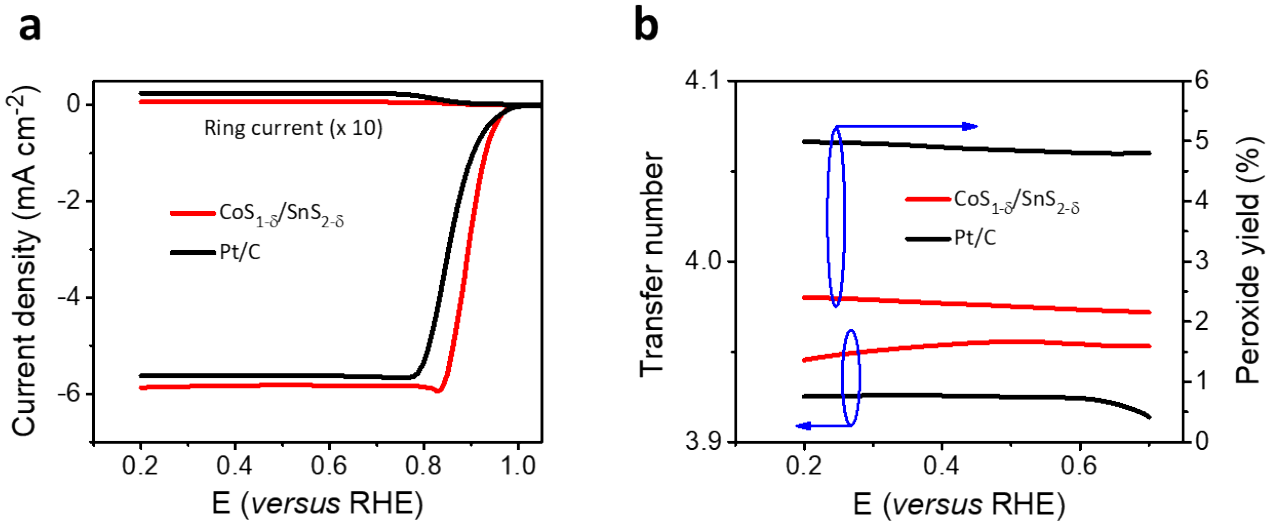

Figure S5. Electrochemical performance. (a) Disc and ring current LSV polarizations for $CoS_{1-\delta}/SnS_{2-\delta}$ and reference Pt/C catalysts. (b) Electron transfer numbers and peroxide yield of $CoS_{1-\delta}/SnS_{2-\delta}$ and reference Pt/C materials from 0.2 to 0.7 V.

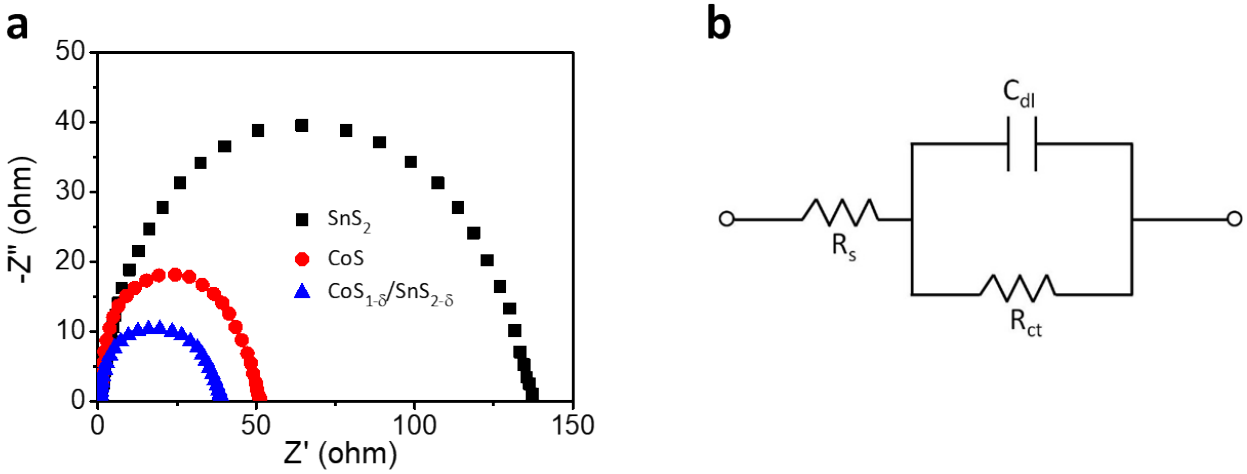

Figure S6. ORR electrochemical kinetics. (a) Electrochemical impedance spectra (EIS) for the SnS_2, CoS, and $CoS_{1-\delta}/SnS_{2-\delta}$ catalysts. (b) Equivalent circuit.

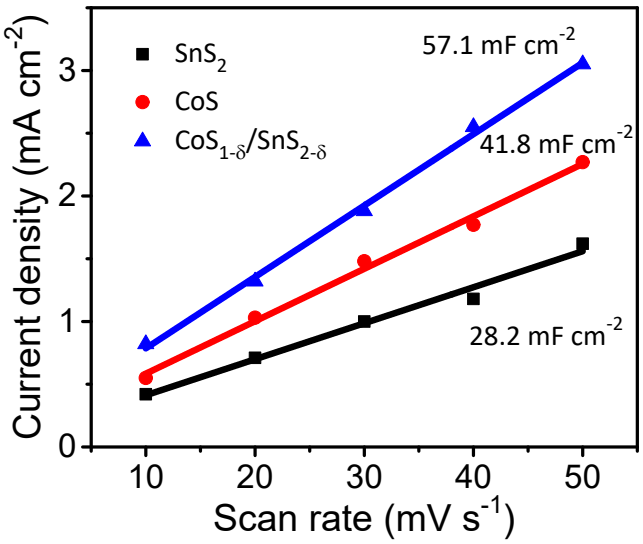

Figure S7. Electrochemical kinetics. Scan rate-dependent current density for CoS, SNS2, and $CoS_{1-\delta}/SnS_{2-\delta}$ catalysts.

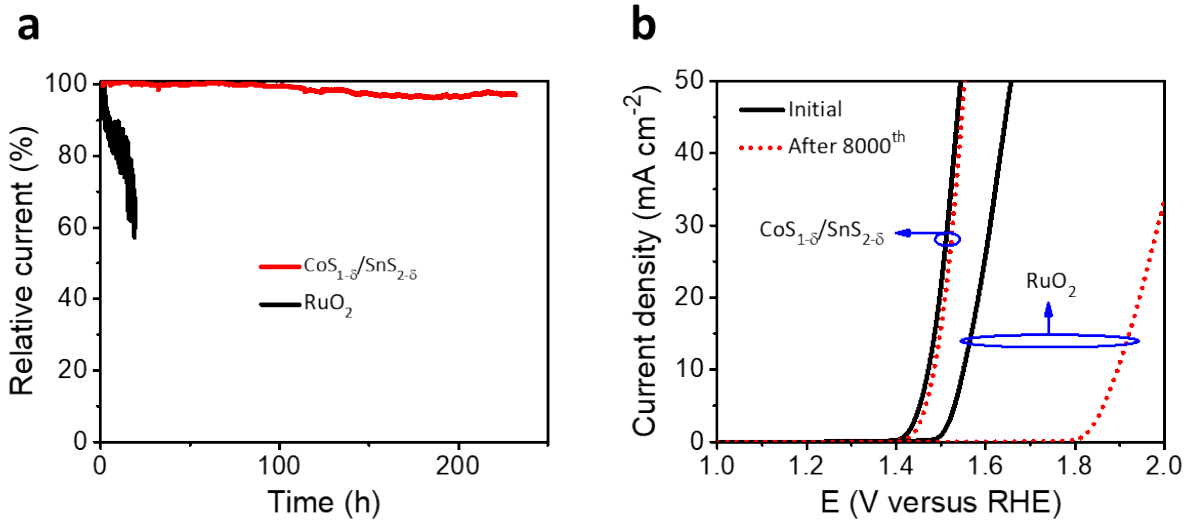

Figure S8. Electrochemical OER stability tests. (a) Comparison of i-t polarizations for $CoS_{1-\delta}/SnS_{2-\delta}$ and RuO_2 for their relevant overpotentials. (b) LSV polarizations for $CoS_{1-\delta}/SnS_{2-\delta}$ and RuO_2 catalysts for initial and after 8,000th cycles.

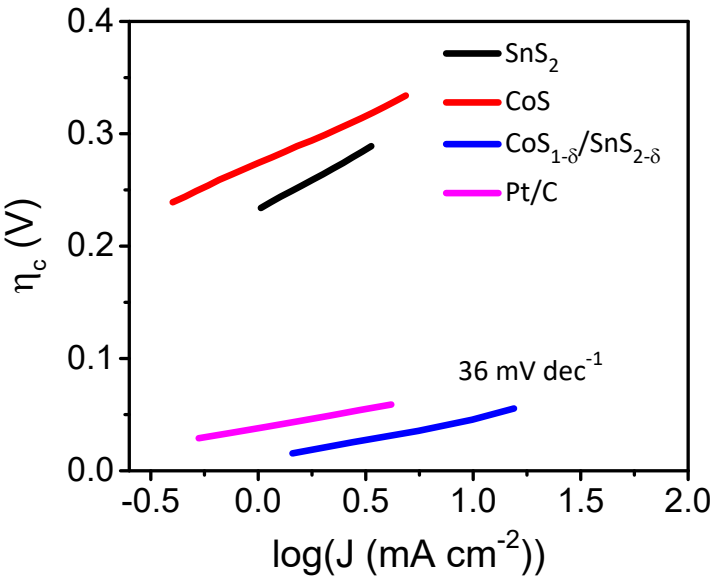

Figure S9. Electrochemical activity. Tafel slopes of different catalysts for HER reactions.

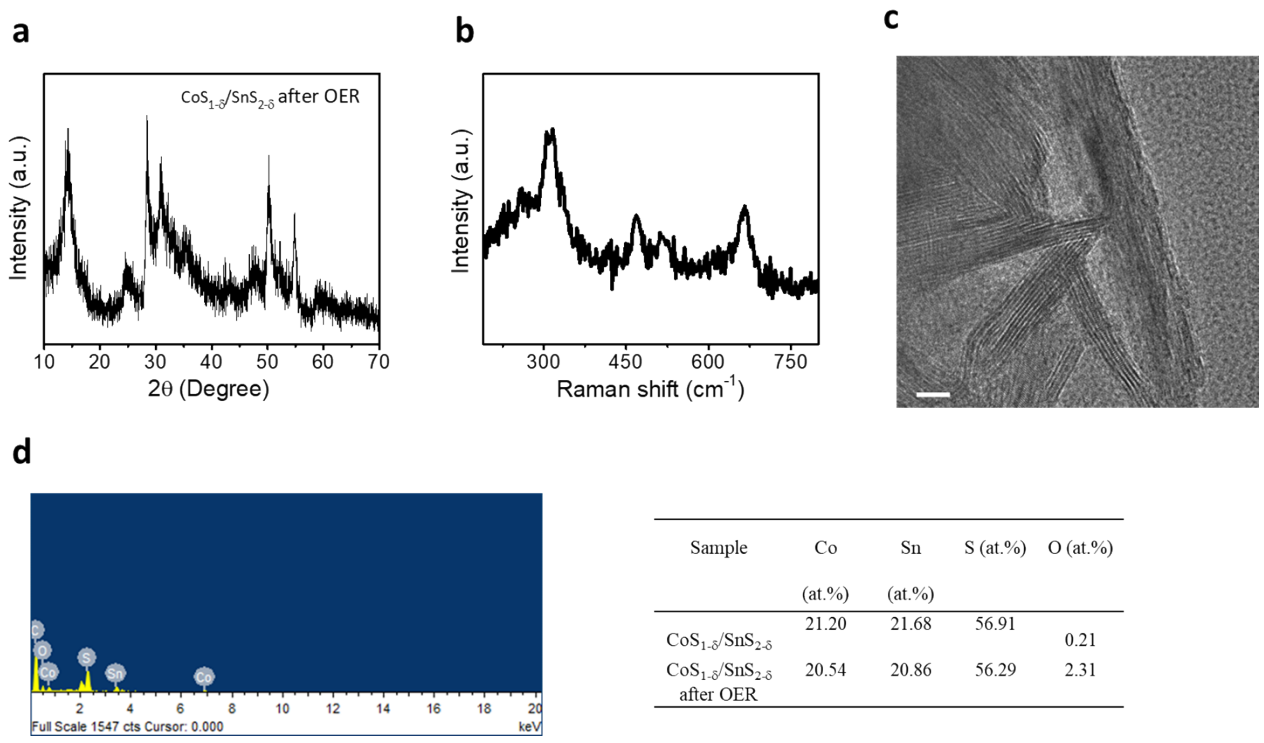

Sample	Co (at.%)	Sn (at.%)	S (at.%)	O (at.%)
$CoS_{1-\delta}/SnS_{2-\delta}$	21.20	21.68	56.91	0.21
$CoS_{1-\delta}/SnS_{2-\delta}$ after OER	20.54	20.86	56.29	2.31

Figure S10. Post-characterizations. (a) XRD pattern, (b) Raman, spectra, (c) HRTEM image, and EDS contents of $CoS_{1-\delta}/SnS_{2-\delta}$ after OER. Scale- 5 nm

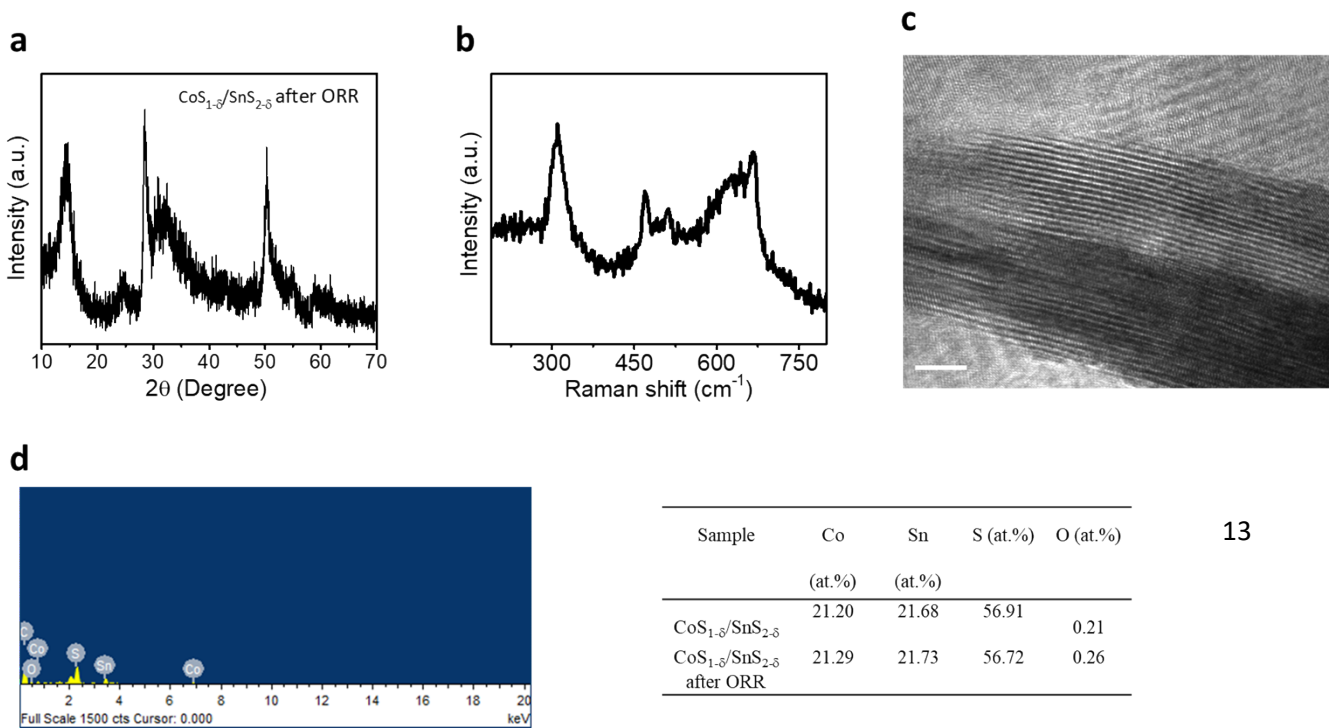

Sample	Co (at.%)	Sn (at.%)	S (at.%)	O (at.%)
$CoS_{1-\delta}/SnS_{2-\delta}$	21.20	21.68	56.91	0.21
$CoS_{1-\delta}/SnS_{2-\delta}$ after ORR	21.29	21.73	56.72	0.26

Figure S11. Post-characterizations. (a) XRD pattern, (b) Raman, spectra, (c) HRTEM image, and EDS contents of $CoS_{1-\delta}/SnS_{2-\delta}$ after ORR. Scale- 5 nm

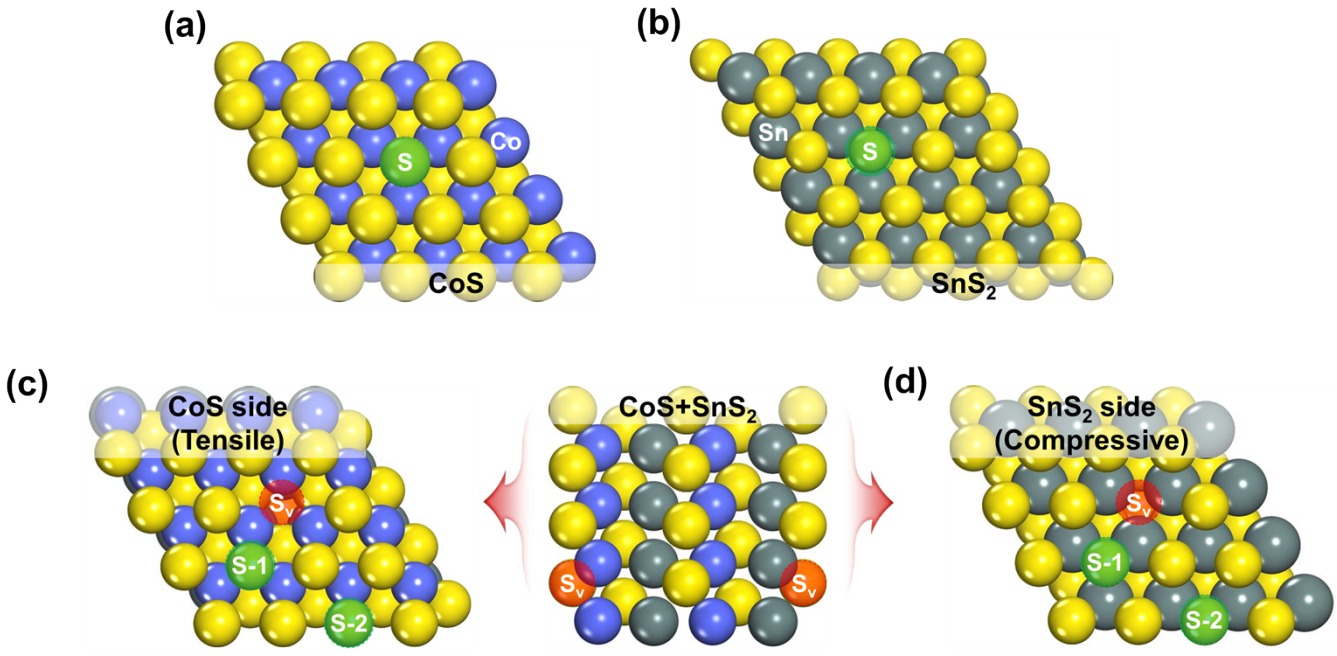

Figure S12. (a) CoS, (b) SnS_2, (c) $CoS_{1-\delta}/SnS_2$, and (b) $CoS/SnS_{2-\delta}$ structures with all possible HER and OER/ORR active sites. Green and red circle indicates S and S defect site. S defect exposes Co and Sn sites.

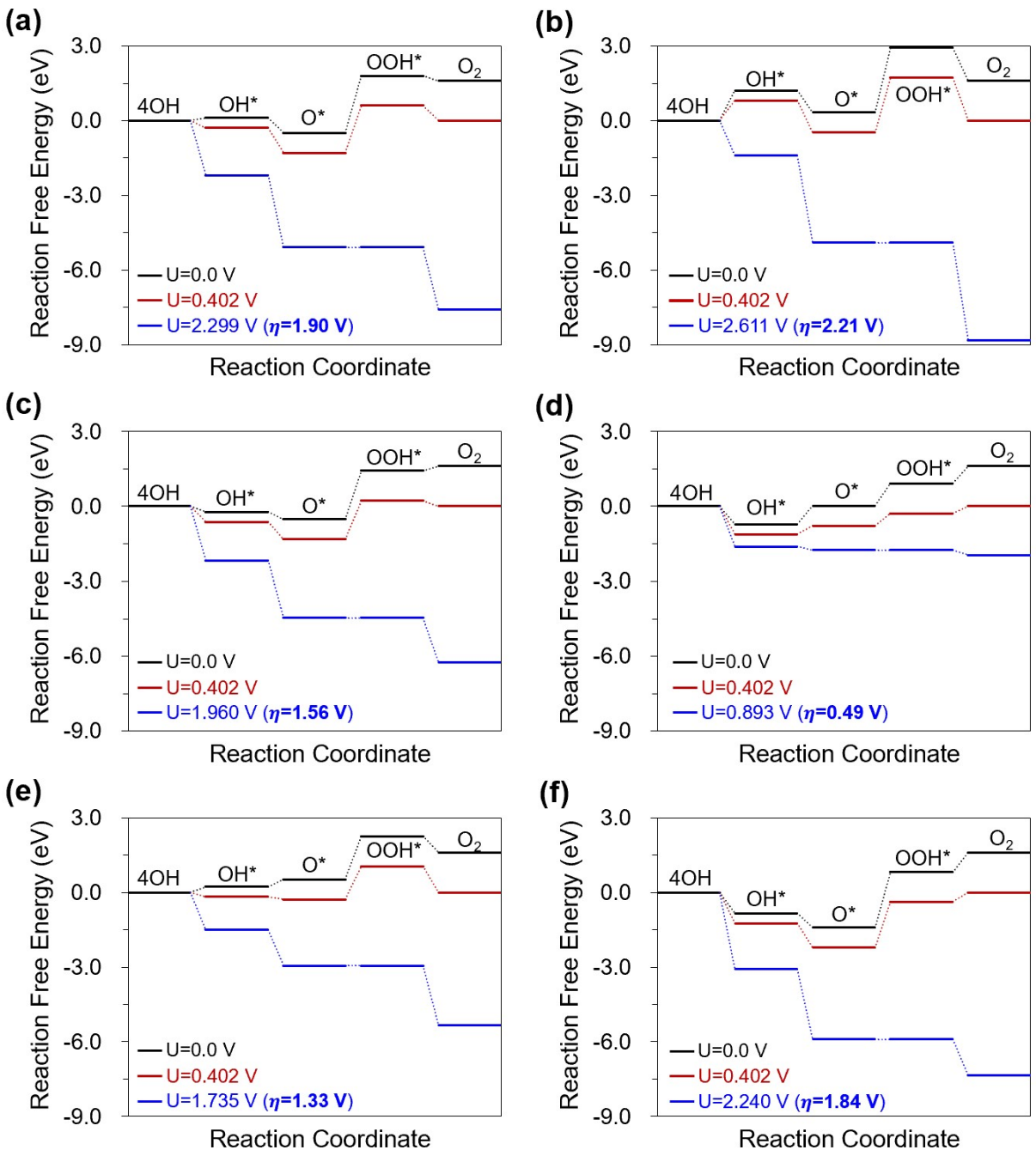

Figure S13. OER free energy diagrams (FEDs) for the (a) S site of CoS, (b) S site of SnS_2, (c) S site of $CoS_{1-\delta}/SnS_2$, (d) S_v (Sn site) of $CoS_{1-\delta}/SnS_2$, (e) S site of $CoS/SnS_{2-\delta}$, and (f) S_v (Sn site) of $CoS/SnS_{2-\delta}$.

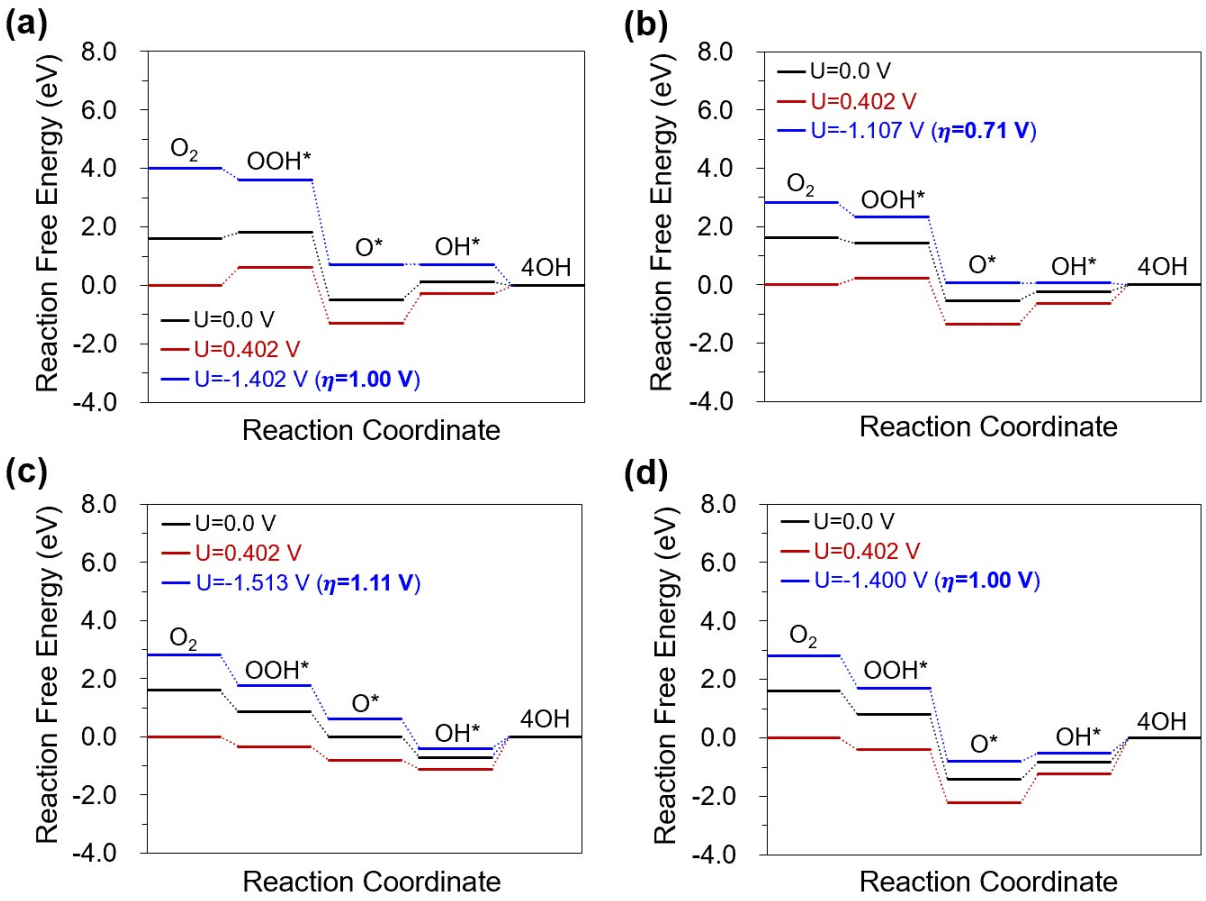

Figure S14. Four-step ORR free energy diagrams (FEDs) for the (a) S site of CoS, (b) S site of $CoS_{1-\delta}/SnS_2$, (c) S_v (Co site) of $CoS_{1-\delta}/SnS_2$, and (d) S_v (Sn site) of $CoS/SnS_{2-\delta}$. The O_2 binding on S sites of $CoS/SnS_{2-\delta}$ and SnS_2 has physisorption leading to an inefficient ORR process, and thus, they are excluded.

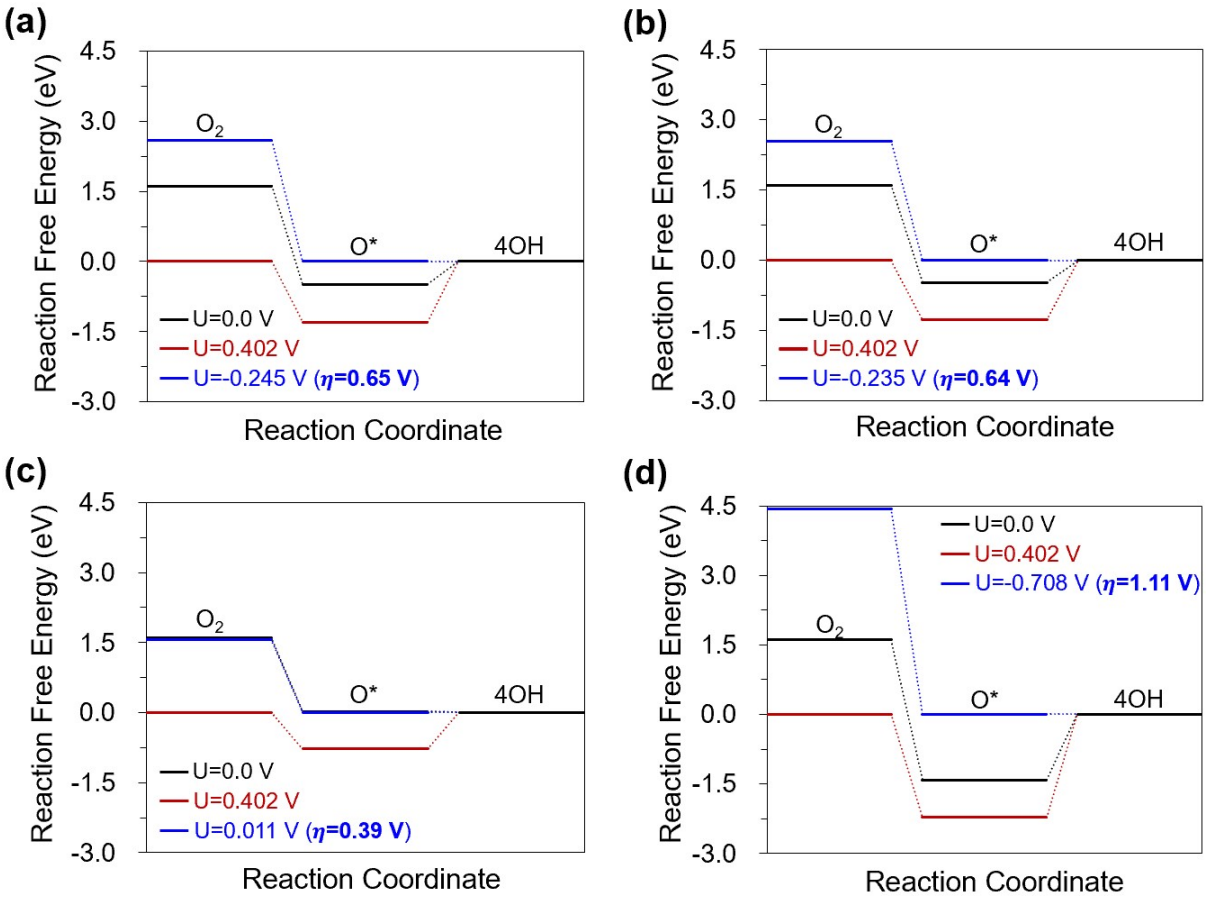

Figure S15. Two-step ORR free energy diagrams (FEDs) for the (a) S site of CoS, (b) S site of $CoS_{1-\delta}/SnS_2$, (c) S_v (Co site) of $CoS_{1-\delta}/SnS_2$, and (d) S_v (Sn site) of $CoS/SnS_{2-\delta}$. The O_2 binding on S sites of $CoS/SnS_{2-\delta}$ and SnS_2 has physisorption leading to an inefficient ORR process, and thus, they are excluded.

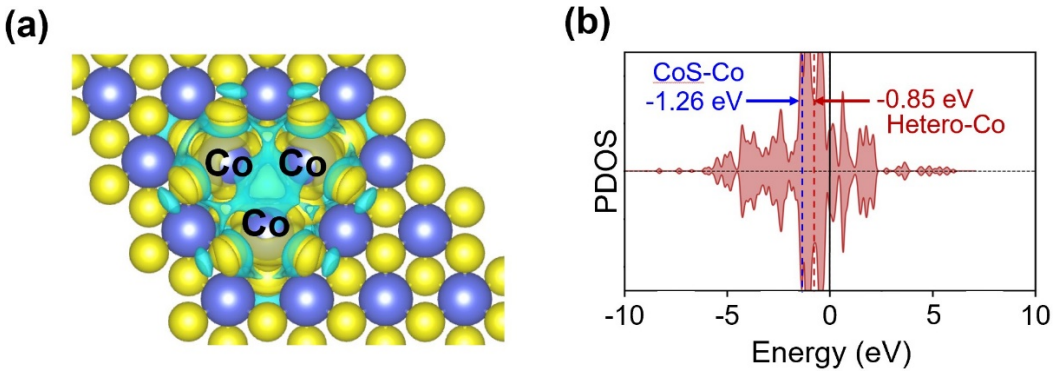

Figure S16. (a) Charge density difference of Co sites generated by S defect and the isosurface level is 0.0015 eÅ^{-3}. Cyan and yellow colors indicate hole and electron, respectively. (b) Partial Density of states (PDOS) for $Co_{d\text{-orbitals}}$ of $CoS_{1-\delta}/SnS_2$ structure. Red and blue dashed lines represent the *d*-band center for Co site of CoS and $CoS_{1-\delta}/SnS_2$, respectively.

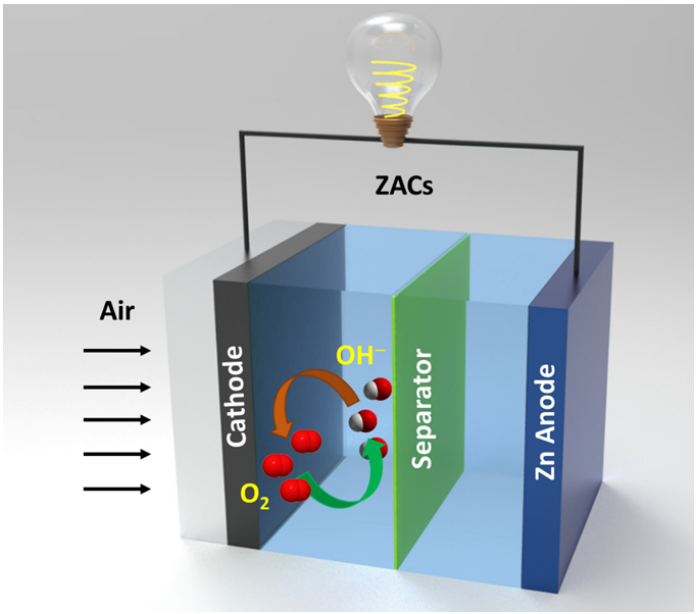

Figure S17. Alkaline cell design. Schematic illustration for alkaline secondary ZABs.

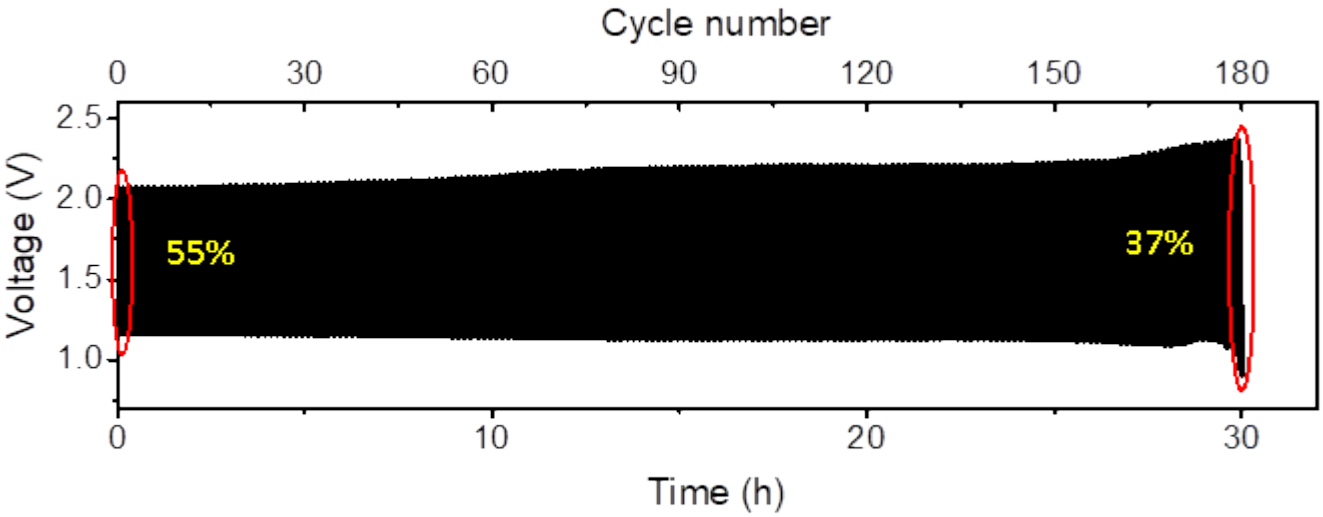

Figure S18. Alkaline ZABs electrochemical performance. Charge-discharge cycle operations for Pt/C + RuO_2 based aqueous ZABs. (Conditions: Current density = 20 mA cm^{-2}, electrolyte = 6 M KOH + 0.2 M Zn acetate)

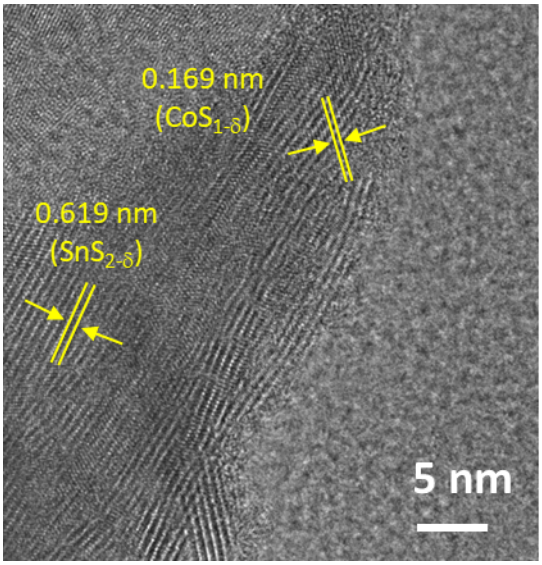

Figure S19. Post microscopic characterizations. HRTEM image of $CoS_{1-\delta}/SnS_{2-\delta}$ cathode after 1008 discharge and charge cycles at 20 mA cm^{-2} for alkaline ZABs.

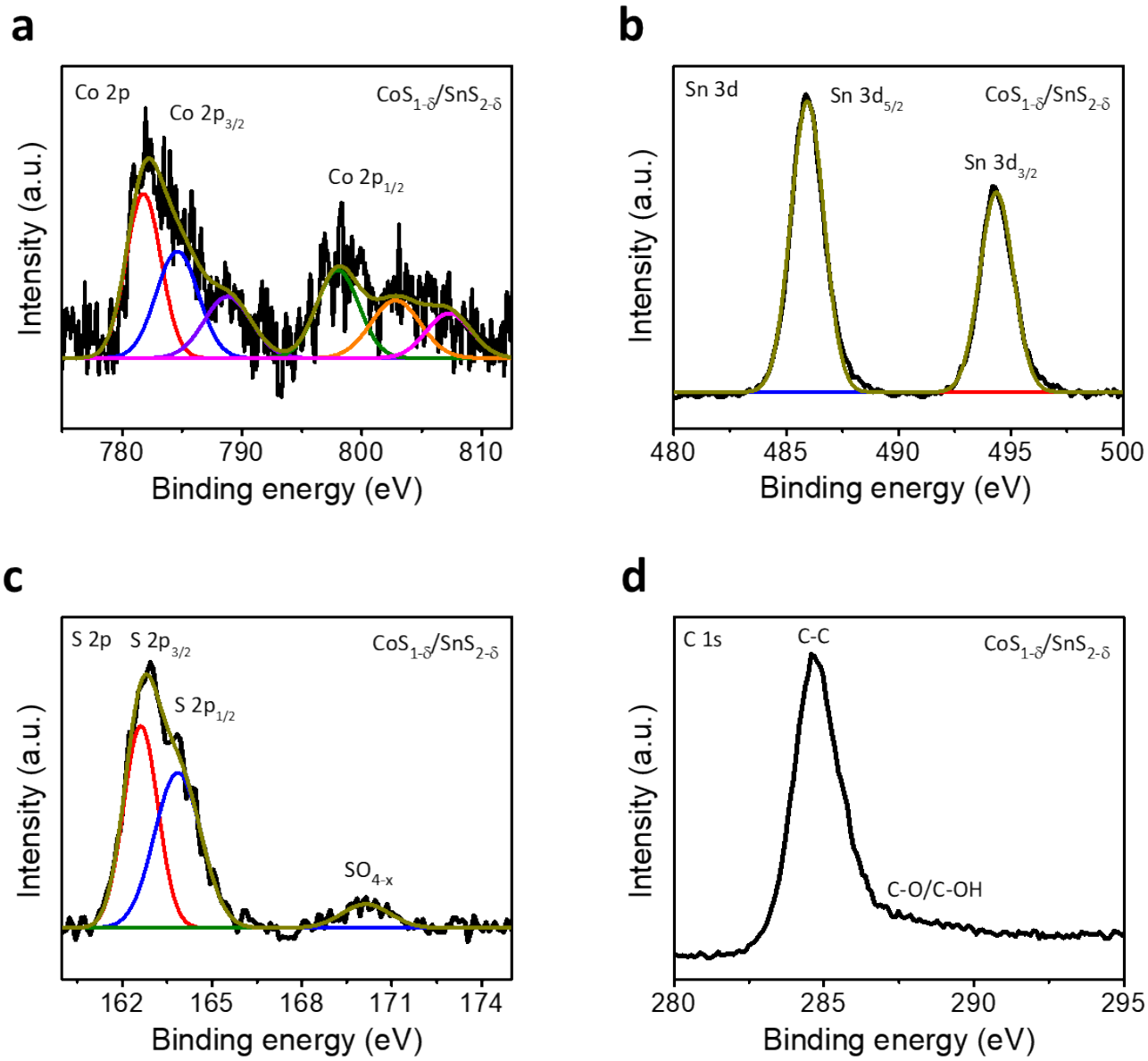
a
Co 2p
Co 2p3/2
Co 2p1/2
CoS1-δ/SnS2-δ
Intensity (a.u.)
780
790
800
810
Binding energy (eV)
b
Sn 3d
Sn 3d5/2
Sn 3d3/2
CoS1-δ/SnS2-δ
Intensity (a.u.)
480
485
490
495
500
Binding energy (eV)
c
S 2p
S 2p3/2
S 2p1/2
SO4-x
CoS1-δ/SnS2-δ
Intensity (a.u.)
162
165
168
171
174
Binding energy (eV)
d
C 1s
C-C
C-O/C-OH
CoS1-δ/SnS2-δ
Intensity (a.u.)
280
285
290
295
Binding energy (eV)

Figure S20. Post spectroscopic characterizations. XPS spectra for $CoS_{1-\delta}/SnS_{2-\delta}$ cathode after 1008 discharge and charge cycles for alkaline ZABs at 20 mA cm^{-2}. (a) Co 2p, (b) Sn 3d, (c) S 2p, and (d) C 1s.

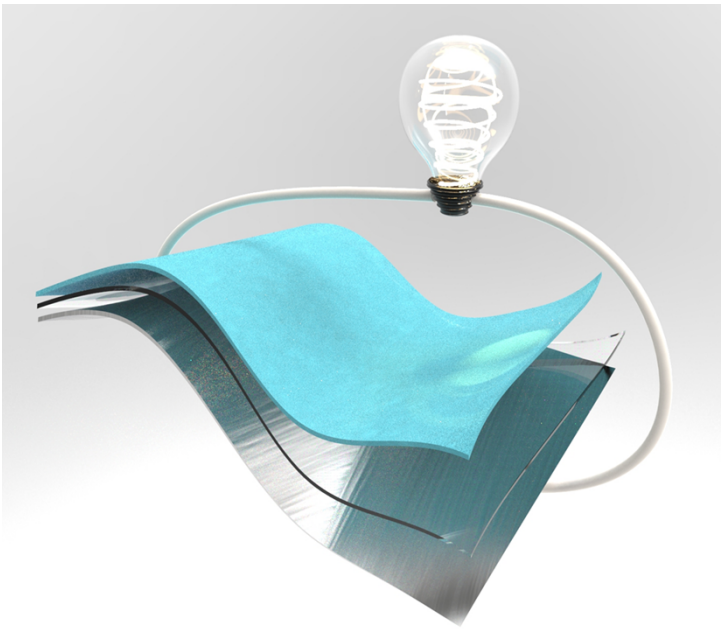

Figure S21. Flexible ZABs assembly. Design structure for flexible solid-state ZABs.

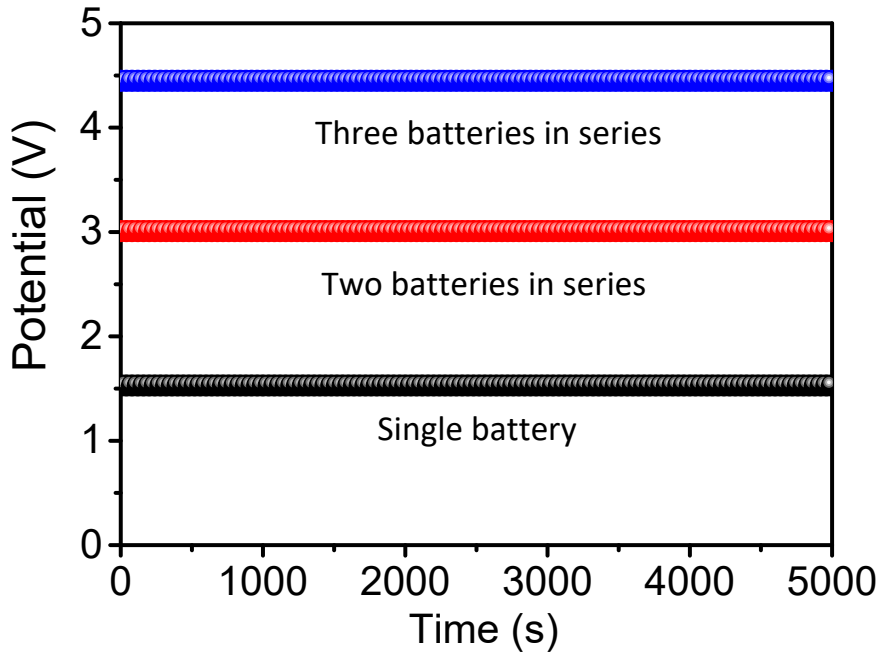

Figure S22. Electrochemical performance. Open circuit potentials (OCPs) for the designed $CoS_{1-\delta}/SnS_{2-\delta}$ cathode based flexible ZABs for serial connections of one, two, and three cells.

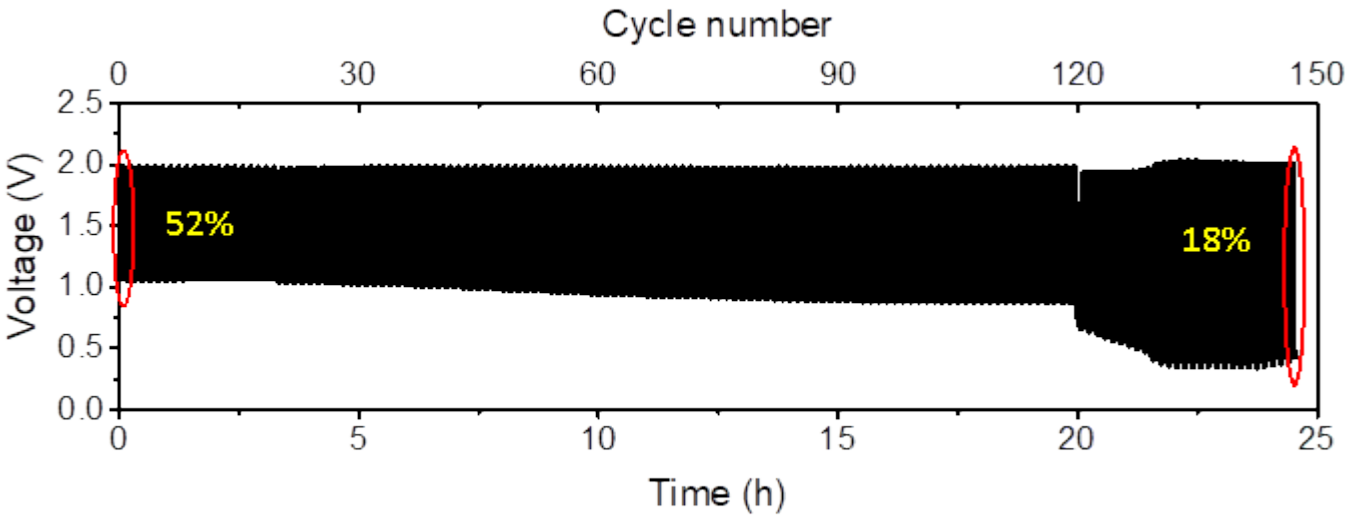

Figure S23. Flexible ZABs electrochemical performance. Galvanostatic cycle operations for Pt/C + RuO_2 based flexible Zn-air cells for the current rate of 50 mA cm^{-2} (Time: 10 min per cycle).

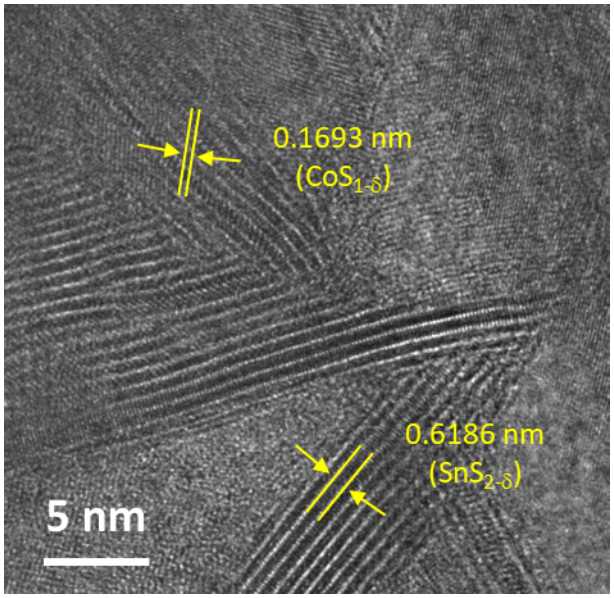

Figure S24. Post microscopic characterizations. HRTEM image of $CoS_{1-\delta}/SnS_{2-\delta}$ cathode after 690 discharge–charge cycle operations for flexible ZABs at 50 mA cm^{-2}.

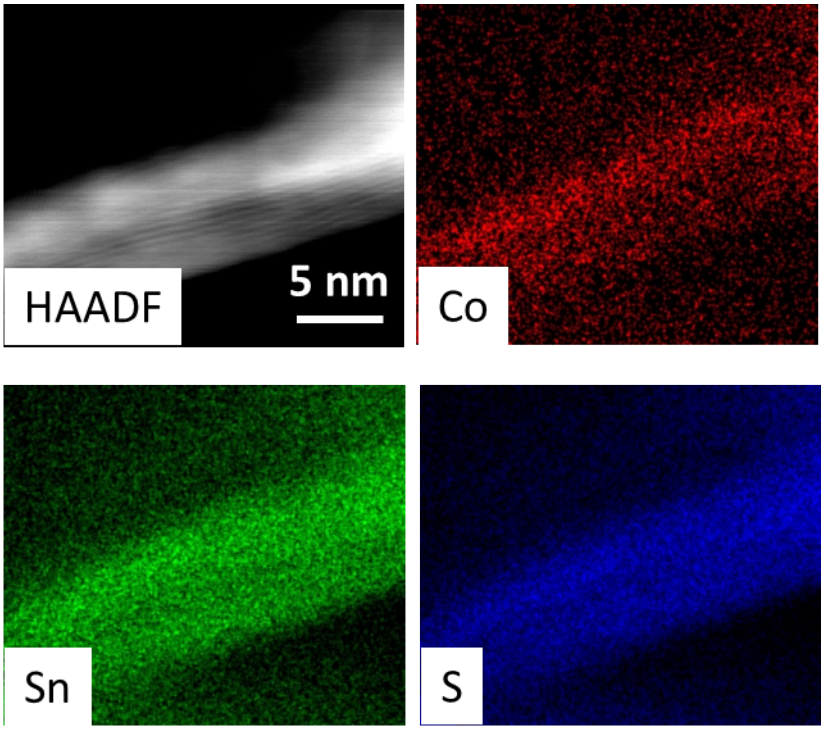

Figure S25. Elemental characterizations. HAADF image and elemental maps of $CoS_{1-\delta}/SnS_{2-\delta}$ cathode after 690 discharge–charge cycle operations for flexible ZABs at 50 mA cm^{-2}.

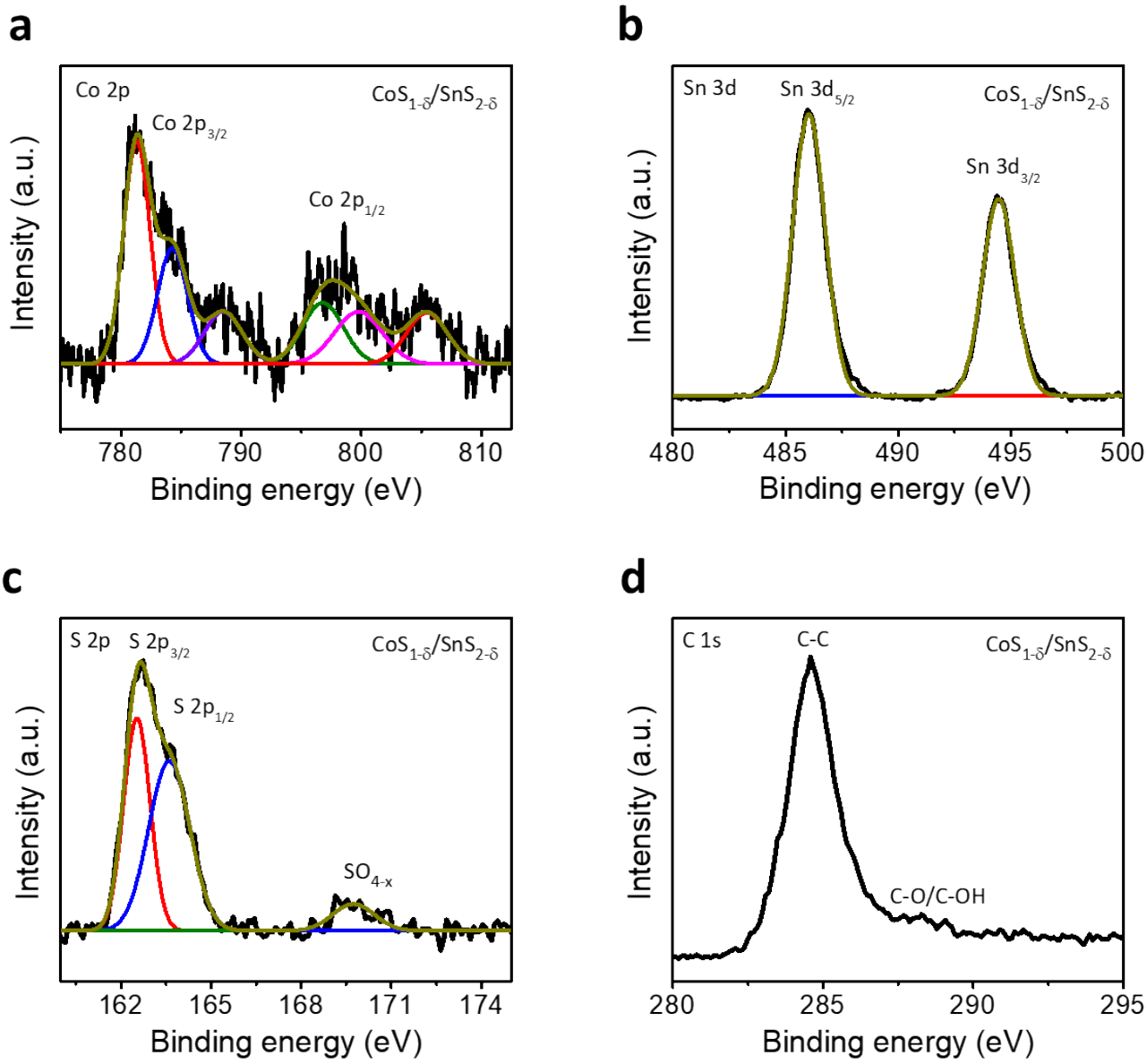
a
Co 2p
Co 2p3/2
Co 2p1/2
CoS1-δ/SnS2-δ
Intensity (a.u.)
780
790
800
810
Binding energy (eV)
b
Sn 3d
Sn 3d5/2
Sn 3d3/2
CoS1-δ/SnS2-δ
Intensity (a.u.)
480
485
490
495
500
Binding energy (eV)
c
S 2p
S 2p3/2
S 2p1/2
SO4-x
CoS1-δ/SnS2-δ
Intensity (a.u.)
162
165
168
171
174
Binding energy (eV)
d
C 1s
C-C
C-O/C-OH
CoS1-δ/SnS2-δ
Intensity (a.u.)
280
285
290
295
Binding energy (eV)

Figure S26. Post spectroscopic characterizations. XPS spectra for $CoS_{1-\delta}/SnS_{2-\delta}$ cathode after 690 discharge-charge operations at 50 mA cm^{-2} for flexible ZABs. (a) Co 2p, (b) Sn 3d, (c) S 2p, and (d) C 1s.

Supplementary Tables

Table S1. Quantitative elemental statistics for the prepared catalysts based on the SEM-EDS analysis.

Sample	Co (at.%)	Sn (at.%)	S (at.%)	S vacancies (%)
SnS_2	-	33.19	66.81	-
CoS	49.89	-	50.11	-
$CoS_{1-\delta}/SnS_{2-\delta}$	21.20	21.68	56.91	0.1545

Table S2. Composition estimation of Co, Sn, and S elements in the fabricated different catalysts based on the SEM-EDS analysis.

Sample	Co (at.%)	Sn (at.%)	S (at.%)	S vacancies (ratio)
$Co_{0.2}S_{1-\delta}/Sn_{1.8}S_{2-\delta}$	4.91	38.83	56.16	0.192
$Co_{0.6}S_{1-\delta}/Sn_{1.4}S_{2-\delta}$	14.44	28.45	57.01	0.1495
$CoS_{1-\delta}/SnS_{2-\delta}$	21.20	21.68	56.91	0.1545
$Co_{1.4}S_{1-\delta}/Sn_{0.6}S_{2-\delta}$	29.40	14.00	56.43	0.1785
$Co_{1.8}S_{1-\delta}/Sn_{0.2}S_{2-\delta}$	39.46	4.87	55.47	0.2265

Table S3. Composition influence of Co and Sn ratio in the $CoS_{1-\delta}/SnS_{2-\delta}$ based catalysts for overall oxygen bifunctional performances.

Catalysts	Overall oxygen bifunctional activity ΔE (V)
$Co_{0.2}S_{1-\delta}/Sn_{1.8}S_{2-\delta}$	1.41
$Co_{0.6}S_{1-\delta}/Sn_{1.4}S_{2-\delta}$	0.97
$CoS_{1-\delta}/SnS_{2-\delta}$	0.57
$Co_{1.4}S_{1-\delta}/Sn_{0.6}S_{2-\delta}$	0.79
$Co_{1.8}S_{1-\delta}/Sn_{0.2}S_{2-\delta}$	1.03

Table S4. Comparison for bifunctional ORR and OER performance for the fabricated $CoS_{1-\delta}/SnS_{2-\delta}$ and reported champion catalysts.

Catalyst	Loading (mg cm^{-2})	ORR onset potential (V *vs*. RHE)	ORR Tafel slope (mV dec^{-1})	ORR half-wave potential ($E_{1/2}$) (V *vs*. RHE)	OER onset potential (V *vs*. RHE)	OER Tafel slope (mV dec^{-1})	OER potential @ 10 mA cm^{-2} ($E_{j=10}$) (V *vs*. RHE)	Overall oxygen electrode activity ΔE ($E_{j=10} - E_{1/2}$) (V)	References
$CoS_{1-\delta}/SnS_{2-\delta}$	0.10	-	46	0.90	-	55	1.47	0.57	This work
PEMAC@NDCN	0.15	-	42	0.87	-	48	1.48	0.61	S5
Mn/Fe-HIB-MOF	0.15	0.98	36	0.883	1.33	45	1.51	0.63	S6
Fe/SNCFs-NH_3	-	-	70.82	0.89	-	-	1.78	0.89	S7
CPS(101)	0.1	0.99	39	0.90	1.38	58	1.49	0.59	S8
FeCo SAs@Co/N-GC	0.25	0.98	49	0.88	1.44	56.6	1.52	0.64	S9
Ir@Co_3O_4[a]	0.5	-	-	0.75	-	-	1.51	0.76	S10
Ni SAs-NC[a]	0.1	-	-	0.85	-	62	1.67	0.82	S11
Co-FPOH[a]	0.283	0.82	183	0.69	-	63	1.52	0.83	S12
Co@IC/MoC@PC	0.4	-	78	0.875	-	82	1.51	0.635	S13
Nitride/N-Ti_3C_2	1.0	0.95	-	0.84	1.48	72	1.53	0.69	S14
IOSHs-NSC-Co_9S_8	1	-	-	0.82	-	101	1.64	0.82	S15
NPMC-1000	0.10	0.94	-	0.85	1.30	-	-	-	S16
NiO/CoN PINWs	0.20	0.89	35	0.68	1.53	-	1.53	0.85	S17

PS-CNS	0.15	0.97	61	0.87	1.26	64	1.56	0.69	S18
Co_4N/CNW/CC	0.20	0.89	-	0.80	1.50	81	1.54	0.74	S19
CCO@C	0.2	0.95	-	0.86	1.47	74	1.56	0.70	S20
1100-CNS	0.42	0.99	58	0.88	1.50	292	1.69	0.81	S21
C-MOF-C2-900	0.5	0.92	-	0.817	1.50	79	1.58	0.763	S22
Co-N,B-CSs	0.1	0.89	64	0.83	1.42	-	1.66	0.83	S23
S-C_2NA	0.15	0.98	54	0.88	1.28	62	1.53	0.65	S24
FeN_x-PNC	0.14	0.99	-	0.86	1.56	80	1.63	0.77	S25
CFZr(0.3)/N-rGO	0.3	0.85	-	0.76	1.4	-	1.6	0.84	S26
NDGs-800	0.2	0.98	81	0.85	1.5	132	1.68	0.83	S27
CMO/S-300	0.3	0.915	52	0.76	1.5	-	1.70	0.94	S28
Co/Co_3O_4@PGS	0.3	0.97	52.6	0.89	1.52	76.1	1.58	0.69	S29
DN-CP@G	0.2	0.95	-	0.801	1.5	65	1.788	0.987	S30
N-GRW	0.30	0.92	53	0.84	1.53	47	1.59	0.75	S31
NCNF-1000	0.10	0.94		0.85	1.30		1.84	1.02	S32
$NiCo_2S_4$/N-CNT	0.25	0.93	-	0.80	-	-	1.60	0.80	S33
NC-Co_3O_4-90	1.2	0.91	-	0.87	-	-	1.59	0.72	S34
FeNi@N-GR	0.2	0.94	-	0.83	1.38	62	1.44	0.61	S35
PS-CNF	0.2	0.95	29	0.86	1.32	89	1.55	0.69	S36

S,N-Fe/N/C-CNT	0.25	0.94	-	0.84	1.45	82	1.60	0.76	S37
Co_3O_4/NPGC	0.20	0.97	-	0.84	1.45	-	1.68	0.84	S38
PCN-CFP	0.20	0.94	122.3	0.67	1.53	61.6	1.63	0.96	S39
N-GCNT/FeCo-3	0.40	1.03	66.8	0.92	1.42	99.5	1.73	0.81	S40
CoO/N-G	0.70	0.90	48	0.81	1.30	71	1.57	0.76	S41

Table S5. Comparison for HER activities for the fabricated $CoS_{1-\delta}/SnS_{2-\delta}$ and reported champion catalysts. (Electrolyte conditions- a. 0.1 M KOH, b. 1 M KOH)

Catalyst	Loading (mg cm^{-2})	Onset potential (V *vs*. RHE)	Current density (mA cm^{-2})	Overpotential at j (mV)	HER Tafel slope (mV dec^{-1})	References
$CoS_{1-\delta}/SnS_{2-\delta}$[a]	0.2	-	10	41	36	This work
CPS (101)[a]	0.2	-0.015	10	39	26	S8
NOGB-800[b]	0.4	-	10	220	98	S42
GHBGQD2[a]	-	-0.08	10	130	95	S43
Co/CNF (1000)[b]	0.3		10	190	66	S44
Co-Co_9S_8@SN-CNTs-900[a]	0.4	-0.12	10	230	92	S45
Ru@C_2N[a]	0.285		10	17	38	S46
			15	27		
			20	35.5		
$CoMoS_x$[a]	0.050	-	5	~158	-	S47
np-CuTi[a]	-	-	10	~47	110	S48
NF/NiMoO-H_2[b]	4.5	-	10	11	43	S49
			100	53		
MoS_x@NiO[b]	-	-	10	406	43	S50
CoP NWs 40s/CC[b]	-	-	100	150	43	S51
NPNNS[b]	0.2	-	10	87	69	S52
$CoSe_{1.26}P_{1.42}$[b]	0.3	-	100	~200	90	S53
Mo_2C nanobelts[b]	0.5	-	10	110	49.7	S54
Ru-RuO_2/CNT[b]	0.3	-0.012	10	23	30	S55
FeCoNiSx	-	-	10	174	-	S56

CoN_4-C	-	-	10	94	55.4	S57

Table S6. ΔG_1 free energies by the ORR four-step (associative) and two-step (Langmuir-Hinshelwood, LH) pathways, which are related to the relative stabilities of the OOH* and O* intermediates generated after the adsorption of O_2, respectively.

Structures	Active sites	ΔG_1 (Associative)	ΔG_1 (LH)
CoS	S	0.20	-2.10
	S-1	-0.04	-2.08
$CoS_{1-\delta}/SnS_2$	S-2	-0.18	-2.14
	S_v (Co site)	-0.74	-1.59
$CoS/SnS_{2-\delta}$	S_v (Sn site)	-0.81	-3.02

Table S7. Comparison of $CoS_{1-\delta}/SnS_{2-\delta}$ based ZABs performance in the alkaline electrolytes compared to those of previously reported champion materials.

Catalyst	OCP (V)	Power density (mW cm^{-2})	Specific capacity (mAh g^{-1})	Energy density (Wh kg^{-1})	Durability (h)	References
$CoS_{1-\delta}/SnS_{2-\delta}$	1.53	249	814	1066	-	This work
PEMAC@NDCN	1.51	214	817	1070	-	S5
Pt/C +RuO_2	1.5	178	773	966	-	S5
Mn/Fe-HIB-MOFs	1.50	195	768	1027	-	S6
Fe/SNCFs-NH_3	-	255	-	-	-	S7
FeCo SAs@Co/N-GC	-	207	741	934	-	S9
Co-FPOH	-	167.8	817	980	-	S12
Co@IC/MoC@PC	-	221	728	-	-	S13
Nitride/N-Ti_3C_2	-	27	630	756	-	S14
PFN PF	-	175	816	938	-	S58
Co_9S_8@N,S-C	-	259	862	-	-	S59
FeCo/Se-CNT	-	175	750	894	-	S60
Co-TMPyP/CCG	-	225	793	-	-	S61
NPMC-1000	1.48	55	735	-	240 (~1.3 V)	S16
NiO/CoN PINWs	1.46	79.6	690	945	-	S17
P,S-CNS	1.51	198	830	-	210 (~1.3 V)	S18

Co_4N/CNW/CC	1.40	174	774	944	-	S19
1100-CNS	1.49	151	-	-	100 (~ 1.3 V)	S21
C-MOF-C2-900	1.43	105	768	998	-	S22
Co-N,B-CSs	1.43	100.4	-	-	-	S23
S-C_2NA	1.49	209	863	958	-	S24
FeNx-PNC	1.55	278	-	-	-	S25
CFZr(0.3)/N-rGO	1.39	-	732	-	-	S26
NDGs-800	1.45	115.2	750.8	-	-	S27
CMO/S-300	1.5	152	-	-	-	S28
Co/Co_3O_4@PGS	1.45	118.27	-	-	-	S29
DN-CP@G	1.43	135	591	-	-	S30
N-GRW	1.46	65	873	-	-	S31
NCNF-1000	1.48	185	660	776	-	S32
NC-Co_3O_4-90	1.44	-	-	-	-	S33
FeNi@N-GR	1.48	85	765	920	-	S34
PS-CNF	1.49	231	698	907	240 (~1.3 V)	S36
S-GNS/$NiCo_2S_4$	1.38	216.3	-	-	-	S62
CNT@POF	1.49	237	772.7	-	-	S63
$PbMnO_x$	-	40	-	-	50 (~1.2 V)	S64

N, B-CNT	-	25	-	-	30 (~1.1 V)	S65
NiC_2O_4	-	-	580	-	10 (~1.25 V)	S66
FePc-Py-CNTs	-	-	-	-	100 (~1.2 V)	S67
CoO/N-CNT	1.40	265	570	-	-	S68
CuPt-NC	1.50	250	560	-	-	S69
MnO_x/C	1.40	190	290	-	-	S70
CuS/NiS_2	1.44	172.4	775	-	-	S71

Table S8. Comparison of cycle life operations for $CoS_{1-\delta}/SnS_{2-\delta}$ based ZABs in the alkaline electrolyte compared to those of previous reports.

Catalyst	Rechargeability	Reference
$CoS_{1-\delta}/SnS_{2-\delta}$	600 s/cycle for >1008 cycles; 168 h@20 mA cm^{-2}	This work
PEMAC@NDCN	600 s/cycle for 2160 cycles; 360 h@20 mA cm^{-2}	S5
Mn/Fe-HIB-MOFs	600 s/cycle for 6000 cycles; 1000 h@10 mA cm^{-2}	S6
Fe/SNCFs-NH_3	3600 s/cycle for 1000 cycles; 1000 h@1 mA cm^{-2}	S7
FeCo SAs@Co/N-GC	600 s/cycle for 1200 cycles; 200 h@10 mA cm^{-2}	S9
Ir@Co_3O_4	1200 s/cycle for 720 cycles; 240 h@10 mA cm^{-2}	S10
Co-FPOH	600 s/cycle for 1200 cycles; 450 h@5 mA cm^{-2}	S12
Co@IC/MoC@PC	1200 s/cycle for 300 cycles; 100 h@1 mA cm^{-2}	S13
Nitride/N-Ti_3C_2	3600 s/cycle for 120 cycles; 120 h@20 mA cm^{-2}	S14
PFN PF	1800 s/cycle for 1000 cycles; 500 h@20 mA cm^{-2}	S42
Co_9S_8@N,S-C	720 s/cycle for 660 cycles; 110 h@1 mA cm^{-2}	S43
FeCo/Se-CNT	1200 s/cycle for 210 cycles; 70 h@5 mA cm^{-2}	S44
Co-TMPyP/CCG	1200 s/cycle for 300 cycles; 100 h@2 mA cm^{-2}	S45
NPMC-1000	600 s/cycle for 600 cycles; 100 h@2 mA cm^{-2}	S16
NiO/CoN PINWs	600 s/cycle for 25 cycles; 8.3 h@50 mA cm^{-2}	S17
P,S-CNS	720 s/cycle for 500 cycles; 100 h@2 mA cm^{-2}	S18
Co_4N/CNW/CC	1200 s/cycle for 408 cycles; 136 h@10 mA cm^{-2}	S19
CCO@C	1800 s/cycle for 160 cycles; 80 h @2 mA cm^{-2}	S20
1100-CNS	660 s/cycle for 300 cycles; 55 h @10 mA cm^{-2}	S21
C-MOF-C2-900	1200 s/cycle for 360 cycles; 120 h @2 mA cm^{-2}	S22
Co-N,B-CSs	394 s/cycle for 128 cycles; 14 h @5 mA cm^{-2}	S23
S-C_2NA	2 h/cycle for 375 cycles; 750 h@10 mA cm^{-2}	S24
FeN_x-PNC	660 s/cycle for 220 cycles; 40 h @5 mA cm^{-2}	S25

CFZr(0.3)/N-rGO	3600 s/cycle for 11 cycles; 11 h @15 mA cm^{-2}	S26
NDGs-800	1200 s/cycle for 234 cycles; 78 h @10 mA cm^{-2}	S27
CMO/S-300	400 s/cycle for 120 cycles; 13 h @5 mA cm^{-2}	S28
Co/Co_3O_4@PGS	600 s/cycle for 4800 cycles; 800 h @10 mA cm^{-2}	S29
DN-CP@G	3600 s/cycle for 250 cycles; 250 h @5 mA cm^{-2}	S30
N-GRW	1h/cycle for 160 cycles; 160 h@2 mA cm^{-2}	S31
NCNF-1000	600 s/cycle for 500 cycles; 83 h@10 mA cm^{-2}	S32
$NiCo_2S_4$/N-CNT	400 s/cycle for 150 cycles; 17 h@10 mA cm^{-2}	S33
NC-Co_3O_4-90	1200 s/cycle for 600 cycles; 200 h@10 mA cm^{-2}	S34
FeNi@N-GR	1200 s/cycle for 120 cycles; 40 h @20 mA cm^{-2}	S35
PS-CNF	700 s/cycle for 600 cycles; 120 h @2 mA cm^{-2}	S36
Co_3O_4/NPGC	1200 s/cycle for 250 cycles; 83 h@5 mA cm^{-2}	S38
PCN-CFP	600 s/cycle for 50 cycles; 8.3 h@20 mA cm^{-2}	S39
N-GCNT/FeCo-3	600 s/cycle for 240 cycles; 40 h@125 mA cm^{-2}	S40
S-GNS/$NiCo_2S_4$	2400 s/cycle for 150 cycles; 100 h @10 mA cm^{-2}	S62
CNT@POF	1200 s/cycle for 200 cycles; 67 h @2 mA cm^{-2}	S63
CoO/N-CNT + NiFe LDH/Ni	10 h/cycle for 10 cycles; 200 h@20 mA cm^{-2}	S68
CuS/NiS_2	1800 s/cycle for 500 cycles; 83 h @25 mA cm^{-2}	S70
macro/meso-NC-NH_3 + COMT@Ni	4 h/cycle for 200 cycles; 800 h@10 mA cm^{-2}	S72
Co_3O_4 NWs	600 s/cycle for 100 cycles; 17 h@50 mA cm^{-2}	S73
NCNT/CoO-NiO-NiCo	600 s/cycle for 100 cycles; 17 h@20 mA cm^{-2}	S74
LBSCFO-50	600 s/cycle for 100 cycles; 17 h@10 mA cm^{-2}	S75
$Ni_{6/7}Fe_{1/7}$-OH-6/CNT	600 s/cycle for 150 cycles; 25 h@15 mA cm^{-2}	S76
NiCo/PFC	2 h/cycle for 300 cycles; 600 h@10 mA cm^{-2}	S77
Ni_3Fe/N-C	4 h/cycle for 105 cycles; 420 h@10 mA cm^{-2}	S78

$NiO/Ni(OH)_2$	70 min/cycle for 70 cycles; 82 h@1 mA cm^{-2}	S79
Fe@NC	600 s/cycle for 100 cycles; 17 h@10 mA cm^{-2}	S80
BNC	600 s/cycle for 66 cycles; 11 h@20 mA cm^{-2}	S81
c-$CoMn_2$/C	400 s/cycle for 155 cycles; 17 h@10 mA cm^{-2}	S82
CCBC-2	600 s/cycle for 75 cycles; 12.5 h@2 mA cm^{-2}	S83
RuSn73	600 s/cycle for 100 cycles; 16.6 h@10 mA cm^{-2}	S84
α-MnO_2/CNT_{10}	300 s/cycle for 100 cycles; 8.33 h@10 mA cm^{-2}	S85

Table S9. Comparison of flexible $CoS_{1-\delta}/SnS_{2-\delta}$ based ZABs performances in reference to those of previous champion catalysts and electrolytes.

Catalyst	Electrolyte	Power density (mW cm^{-2})	Specific capacity (mAh g_{Zn}^{-1})	Energy density (Wh kg_{Zn}^{-1})	Recharge ability	Reference
$CoS_{1-\delta}/SnS_{2-\delta}$	CBCs	229	810	1077	10 min/cycle for >690 cycles; 115 h@50	This work
PEMAC@NDCN	CBCs	211	806	1056	10 min/cycle for 2580 cycles; 430 h@50	S5
Mn/Fe-HIB-MOF	Functionalized Bio-cellulose membrane	193	748	975	10 min/cycle for 3600 cycles; 600 h@25	S6
FeCo SAs@Co/N-GC	Functionalized Bio-cellulose	186	817	1017	10 min/cycle for 684 cycles; 114 h@50	S9
CPS(101)	CBCs	458	-	-	8 min/cycle for 6000 cycles; 800 h@25	S8
Fe/SNCFs-NH_3	(PANa)-KOH-$Zn(CH_3COO)_2$ hydrogel	-	-	-	30 min/cycle for 120 cycles; 60 h@1	S7
FeCo/Se-CNT	PVA gel	37.5	-	-	10 min/cycle for 120 cycles; 20 h@5	S60
Fe_1/d-CN	PVA gel	78	-	-	20 min/cycle for 60	S86

					cycles; 20 h@1	
Nitride/N-Ti_3C_2	PVA gel	27	630	693	60 min/cycle for 120 cycles; 120 h@20	S14
CuSA@HNCNx	Functionalized Bio-cellulose	212	806	1031	10 min/cycle for 1500 cycles; 250 h@ 25	S87
Co_4N/CNW/CC	PVA gel	-	-	-	20 min/cycle for 36 cycles; 12 h	S19
Co-N,B-CSs	PVA gel	-	-	-	6 min/cycle for 230 cycles; 23 h@2	S23
S-C_2NA	Functionalized Cellulose film	187	695	862	30 min/cycle for 900 cycles; 450 h	S24
CMO/S-300	PVA gel	-	-	-	30 min/cycle for 20 cycles; 10 h@1	S28
DN-CP@G	PVA gel	-	530	-	60 min/cycle for 170 cycles; 170 h@1	S30
NCNF-1000	PVA gel	-	378	378	10 min/cycle for 48 cycles; 8 h@1	S32
NC-Co_3O_4-90	Acrylic acid gel	82	387.2	387.2	24 min/cycle for 60 cycles; 24 h@1	S34
FeNi@N-GR	PVA gel	-	-	-	20 min/cycle for 54 cycles; 18 h	S35
N-GCNT/FeCO-3	PVA gel	97.8	-	-	10 min/cycle for 72 cycles; 12 h	S40

CNT@POF	PVA gel	-	-	-	4 min/cycle for 12 cycles; 48 min	S63
CuS/NiS_2	PVA gel	-	-	-	10 min/cycle for 150 cycles; 25 h	S71
Co_3O_4-NCNT/SS	Cellulose film	162	652.6	847.6	20 min/cycle for 1500 cycles; 500 h@25	S88
MnO_x-GCC	Acrylic acid gel	32	-	-	20 min/cycle for 200 cycles; 66.66 h@0.7	S89
Co_3O_4	Cellulose membrane	-	-	-	1 h/cycle for 35 cycles; 35 h@250	S90
$LaNiO_3$/NCNT	PVA gel	56.1	460	581	20 min/cycle for 120 cycles; 40 h@50	S91

Table S10. Flexible ZABs performance comparison for wide temperature operations in reference to those of previous reports.

Catalyst	Electrolyte	Lowest working temperature (°C)	Working temperature (°C)	Power density (mW/cm^2)	Specific capacity (mAh g_{Zn}^{-1})	Energy density (Wh kg_{Zn}^{-1})	Rechargeability @mA cm^{-2}	References
$CoS_{1-\delta}/SnS_{2-\delta}$	CBCs	-40	25	229	810	1077	690 cycles (115 h) @50	This work
			-40	194	685 (85%)	860 (~80%)	264 cycles (44 h) @50	
PEMAC@NDCN	CBCs	-40	70	211	806	1056	2580 cycles (430 h) @50	S5
			-40	165	693 (86%)	738 (~70%)	550 cycles (91 h) @25	
CPS(101)	CBCs	-20	80	458	1.24 Ah	-	6000 cycles (800 h) @25	S8
			-20	-	1 Ah	-	1500 cycles (200 h) @25	
FeMn-DSAC	PAM	-40	25	184	734	888	218 cycles (80 h) @2	S92
			-40	30	631 (86%)	725 (81.6%)	218 cycles (80 h) @2	
NiO/CoO TINWs	PVA	-10	25	-	842	996	33 h @1	S93
			-10	-	328 (39%)	364 (36%)	14 h @1	
Co@NPCP/NBCNF-2-800	PAM	-50	25	165	800	960	600 cycles (100 h) @2	S94
			-50	97	620 (77%)		240 cycles (40 h) @2	

BFC-FC-0.2	PAA	-20	25	160	745	915	600 cycles (105 h) @2	S95
			-20	80	691 (92%)	798 (87%)	-	
Pt/C + Ir/C	KOH	-20	20	126	-	-	210 cycles @5	S96
	CsOH		-20	43	-	-	255 cycles @5	
Pt/RuO_2	PAM	-40	20	43	818	-	75 h @2	S97
			-40	10	743 (90%)	-	40 h @2	
Pt/C and RuO_2	PAM/PAA	-20	25	12	663	769	100 cycles (10 h) @1	S98
			-20	8	506 (76%)	556 (72%)	100 cycles (10 h) @1	

2. Computational details and modeling

All *ab initio* calculations were performed with the Vienna *Ab initio* Simulation Package (VASP 5.4.4).[S99-S102] We used the projector augmented wave (PAW) method[S103-S104] with the generalized gradient approximation based on the Perdew-Burke-Ernzerhof (PBE)[S105] functional (GGA).[S106] A plane-wave cutoff energy of 500 eV was used. Lattice constants and internal atomic positions were fully optimized until the residual forces were less than 0.02 eV/ Å. The spin polarization was also included. Integration in the Brillouin zone was performed based on the Monkhorst-Pack scheme[S107] using a k-point mesh with an interval of 0.05 $Å^{-1}$. For the HER and OER/ORR calculations, we specifically used CoS and SnS_2 with hexagonal phases and $P6_3/mmc$, which can minimize the lattice mismatching. The vacuum slab space of a unit cell in the z-direction was set to 15 Å to avoid interactions between layers. DFT-D3 with BeckeJonson (BJ) damping was used to study the adsorption of intermediates on the surface while considering van der Waals interactions. Further, we investigated the reaction free energies (ΔG) of the elementary steps for the HER and OER/ORR at U=0 V and U=0.402 V (ideal potential), respectively. For the convenience of identifying the active site positions, we name them by element name and Arabic number. The details of the active site naming are also included in Fig. S12. Bader charge analysis is widely used for investigating charge distribution, and it is determined by the zero-gradient surface of electron density between ions. In this study, we performed Bader charge analysis using grid-based charge density decomposition, as developed by Henkelman et al.[S108]

Gibbs free energy calculations for HER and OER/ORR processes

In this work, we used the theoretically well-defined free energy diagram (FED) approach proposed by Norskov group, and computational hydrogen electrode (CHE) model to calculate a reaction free energy for electrochemical reactions. It has been generally accepted approach for the electrochemical studies based on density functional theory (DFT) calculations. Based on this theoretical method, the chemical potential of proton and electron pair ($\mu(H^+ + e^-)$) is estimated from the half of chemical potential of H_2 gas at pH 0, and it can be shifted by $-eU$ when the external potential U is applied, i.e., $\mu(H^+ + e^-) = 0.5\mu(H_2) - eU$. For the investigation of various catalytic reactions on the specific surface structures, we mainly consider

the thermodynamic stabilities of the adsorbents as the main descriptor, which determines the catalytic performance.

Preferentially, the hydrogen evolution reaction (HER) is a multi-step process that generates H_2 gas via two proposed mechanisms, Volmer-Tafel and Volmer-Heyrovsky.

Volmer reaction: $$2H^+ + 2e^- \rightarrow H^* + H^+ + e^- \quad \text{(S6)}$$

Tafel reaction: $$H^* + H^* \rightarrow H_2 + * \quad \text{(S7)}$$

Heyrovsky reaction: $$H^* + H^+ \rightarrow H_2 + * \quad \text{(S8)}$$

where $*$ and H^* indicate the active site and adsorbed H atom on the catalyst surface, respectively. Since the equilibrium reduction potential for the HER is 0.0 V, the chemical potentials of the initial ($2H^+ + 2e^-$) and final states (H_2) should be same. As such, in the case of ideal catalyst, its intermediate state should have the same chemical potential as the initial and final states under equilibrium potential, i.e., U = 0.0 V. However, the actual catalytic cases deviate from the ideal behavior due to the binding strength of the intermediate on the surface of catalyst. Therefore, the optimum value of reaction Gibbs free energy of intermediate (H*) should be zero for a spontaneous reaction without a barrier.

Subsequently, in the case of oxygen evolution reaction (OER), the four electrons/four reaction steps have been generally acceptable, where this process in an alkaline environment can be described as follows.

$$OH^- + * \rightarrow OH^* + e^- \quad \text{(S9)}$$

$$OH^* + OH^- \rightarrow O^* + H_2O(l) + e^- \quad \text{(S10)}$$

$$O^* + OH^- \rightarrow OOH^* + e^- \quad \text{(S11)}$$

$$OOH^* + OH^- \rightarrow * + O_2(g) + H_2O(l) + e^- \quad \text{(S12)}$$

where * refer to the active site, and OH*, O*, and OOH* are adsorbed intermediates on the surface of catalyst.

In contrast to the OER, the ORR can proceed either by a two-step or four-step pathway depending on the relative stabilities of the O * and OOH* intermediates generated after the adsorption of O_2 on the catalyst. The two-step ORR pathway in an alkaline environment is summarized using the following elementary steps:

$$O_2*(g) + H_2O(l) + 2e^- \rightarrow O^* + 2OH^- \quad \text{(S13)}$$

$$O^* + 2OH^- + H_2O(l) + 2e^- \rightarrow * + 4OH^- \quad (S14)$$

whereas the four-step pathway has following elementary steps:

$$O_2^*(g) + H_2O(l) + e^- \rightarrow OOH^* + OH^- \quad (S15)$$

$$OOH^* + e^- \rightarrow O^* + OH^- \quad (S16)$$

$$O^* + H_2O(l) + e^- \rightarrow OH^* + OH^- \quad (S17)$$

$$OH^* + e^- \rightarrow * + OH^- \quad (S18)$$

Considering the elementary reaction steps for the ORR, both reaction pathways lead to the same final products (4OH−), but different intermediate states upon adsorption of O_2 on the catalyst (O * in Eqs. (S13 and S15) and OOH* in Eq. (S16)) are involved. Therefore, it is important to note that the transformations of O_2* to O* in Eq. (S13) or O_2* to OOH* in Eq. (S15) are the important steps that determine which ORR pathway is followed.

To investigate the reaction free energy between each elementary steps including proton and electron transfer, we set the standard reaction conditions (298.15 K and 1 atm) as the reference potential. The ΔG value of each elementary step in the HER and NRR can be obtained by: $\Delta G = \Delta E + \Delta E_{ZPE} - T\Delta S + \Delta G_U + \Delta G_{pH}$, where ΔE that indicates the reaction energy, T is absolute temperature, and ΔE_{ZPE} and ΔS are the change in the zero-point energies and entropy, respectively. And, E_{ZPE} and S values can be computed from the vibrational frequency values of the adsorbed species, which are evaluated from finite-difference calculations. Notably, the entropies of the reference gas molecules (H_2, and H_2O) were taken from the NIST database. ΔG_{pH} is the contribution of H^+, which can be determined as: $\kappa_B T * ln(10) * pH,$ where κ_B is the Boltzmann constant, and in this work, the value of pH was set to 0. ΔG_U indicates the effect of the applied bias at electrode, which is equal to $-neU$, in which n is the number of transferred electrons in each step. So, we used limiting potential (U_L) to assess the NRR catalytic activity, which can be determined by: $U_L = -max(\Delta G_1, \Delta G_2, \Delta G_3, ...,\Delta G_i)/e$, where ΔG_i means the reaction free energy between each elementary step in the whole HER and OER/ORR processes.

Supplementary References

S1 Y. Liang, H. Wang, J. Zhou, Y. Li, J. Wang, T. Regier, H. Dai, *J. Am. Chem. Soc.,* 2012, **134,** 3517–3523.

S2 Paulus, U. Schmidt, T. and Gasteiger, H. R. Behm, *J. Electroanal. Chem.,* 2001, **495,** 134.

S3 S. Zecevic, J. Wainright, M. Litt, S. Gojkovic, R. Savinell, J. Electrochem. Soc., 1997, **144,** 2973–2982.

S4 O. Antoine, R. Durand, *J. Appl. Electrochem.,* 2000, **30,** 839–844.

S5 N. Wagh, S. Shinde, C. Lee, S. Kim, D. Kim, H. Um, S. Lee, J. Lee, *Nano-Micro Lett.*, 2022, **14,** 190.

S6 S. Shinde, C. Lee, J. Jung, N. Wagh, S. Kim, D. Kim, C. Lin, S. Lee, J. Lee, *Energy Environ. Sci.*, 2019, **12,** 727-738.

S7 L. Yang, X. Zhang, L. Yu, J. Hou, Z. Zhou, R. Lv, Adv. Mater. 2105410 (2021).

S8 S. Shinde, J. Jung N. Wagh, C. Lee, S. Kim, S. Lee, J. Lee, Nat. Energy 6, 592-604 (2021).

S9 N. Wagh, D. Kim, S. Kim, S. Shinde, J. Lee, ACS Nano **15,** 14683–14696 (2021).

S10 Y. Dai, J. Yu, J. Wang, Z. Shao, D. Guan, Y. Huang, M. Ni, Adv. Funct. Mater. 2111989 (2022).

S11 H. Jiang, J. Xia, L. Jiao, X. Meng, P. Wang, C. Lee, W. Zhang, Appl. Catal. B: Environ. **310,** 121352 (2022).

S12 L. Song, T. Zheng, L. Zheng, B. Lu, H. Chen, Q. He, W. Zheng, Y. Hou, J. Lian, Y. Wu, J. Chen, Z. Ye, J. Lu, Appl. Catal. B: Environ. **300,** 120712 (2022).

S13 L. Zhang, Y. Zhu, Z. Nie, Z. Li, Y. Ye, L. Li, J. Hong, Z. Bi, Y. Zhou, G. Hu, ACS Nano **15,** 13399−13414 (2021).

S14 Z. Wu, H. Wang, P. Xiong, G. Li, T. Qiu, W. Gong, F. Zhao, C. Li, Q. Li, G. Wang, F. Geng, Nano Lett. **20,** 2892-2898 (2020).

S15 K. Tang, C. Yuan, Y. Xiong, H. Hu, M. Wu, Appl. Catal. B: Environ. **260,** 118209 (2020).

S16 Zhang, J.; Zhao, Z.; Xia, Z.; Dai, L. Nat. Nanotechnol. 2015, **10,** 444-452.

S17 Yin, J.; Li, Y.; Lv, F.; Fan, Q.; Zhao, Y.; Zhang, Q.; Wang, W.; Cheng, F.; Xi, P.; Guo, S. ACS Nano 2017, 11, 2275−2283.

S18 Shinde, S.; Lee, C.; Sami, A.; Kim, D.; Lee, S.; Lee, J. ACS Nano 2017, **11,** 347−357.

S19 Meng, F.; Zhong, H.; Bao, D.; Yan, J.; Zhang X. J. Am. Chem. Soc. 2016, **138,** 10226–10231.

S20 Wang, X.; Li, Y.; Jin, T.; Meng, J.; Jiao, L.; Zhu, M.; Chen, J. Nano Lett. 2017, **17,** 7989−7994.

S21 Pei, Z.; Li, H.; Huang, Y.; Xue, Q.; Huang, Y.; Zhu, M.; Wang, Z.; Zhi, C. Energy Environ. Sci. 2017, **10,** 742-749.

S22 Zhang, M.; Dai, Q.; Zheng, H.; Chen, M.; Dai, L. Adv. Mater. 2018, **30,** 1705431.

S23 Guo, Y.; Yuan, P.; Zhang, J.; Hu, Y.; Amiinu, I.; Wang, X.; Zhou, J.; Xia, H.; Song, Z.; Xu, Q.; Mu, S. ACS Nano 2018, 12, 1894−1901.

S24 Shinde, S.; Lee, C.; Yu, J.; Kim, D.; Lee, S.; Lee, J. ACS Nano 2018, 12, 596–608.

S25 Ma, L.; Chen, S.; Pei, Z.; Huang, Y.; Liang, G.; Mo, F.; Yang, Q.; Su, J.; Gao, Y.; Zapien, J.; Zhi, C. ACS Nano 2018, 12, 1949−1958.

S26 Kashyap, V.; Kurungot, S. ACS Catal. 2018, 8, 3715−3726.

S27 Wang, Q.; Ji, Y.; Lei, Y.; Wang, Y.; Wang, Y.; Li, Y.; Wang, S. ACS Energy Lett. 2018, 3, 1183−1191.

S28 Peng, S.; Han, X.; Li, L.; Chou, S.; Ji, D.; Huang, H.; Du, Y.; Liu, J.; Ramakrishna, S. Adv. Energy Mater. 2018, 8, 1800612.

S29 Jiang, Y.; Deng, Y.; Fu, J.; Lee, D.; Liang, R.; Cano, Z.; Liu, Y.; Bai, Z.; Hwang, S.; Yang, L.; Su, D.; Chu, W.; Chen, Z. Adv. Energy Mater. 2018, 8, 1702900.

S30 Hang, C.; Zhang, J.; Zhu, J.; Li, W.; Kou, Z.; Huang. Y. Adv. Energy Mater. 2018, 8, 1703539.

S31 Yang, H.; Miao, J.; Hung, S.; Chen, J.; Tao, H.; Wang, X.; Zhang, L.; Chen, R.; Gao, J.; Chen, H.; Dai, L.; Liu, B. Sci. Adv. 2016, 2, e1501122.

S32 Liu, Q.; Wang, Y.; Dai, L.; Yao, J. Adv. Mater. 2016, 28, 3000–3006.

S33 Han, X.; Wu, X.; Zhong, C.; Deng, Y.; Zhao, N.; Hu, W. Nano Energy 2017, 31, 541–550.

S34 Guan, C.; Sumboja, A.; Wu, H.; Ren, W.; Liu, X.; Zhang, H.; Liu, Z.; Cheng, C.; Pennycook, S.; Wang, J. Adv. Mater. 2017, 29, 1704117.

S35 Liu, P.; Gao, D.; Xiao, W.; Ma, L.; Sun, K.; Xi, P.; Xue, D.; Wang, J. Adv. Funct. Mater. 2018, 28, 1706928.

S36 Shinde, S.; Yu, J.; Song, J.; Nam, Y.; Kim, D.; Lee, J. Nanoscale Horiz. 2017, 2, 333-341.

S37 Chen, P.; Zhou, T.; Xing, L.; Xu, K.; Tong, Y.; Xie, H.; Zhang, L.; Yan, W.; Chu, W.; Wu, C.; Xie, Y. Angew. Chem., Int. Ed. 2017, 56, 610–614.

S38 Li, G.; Wang, X.; Fu, J.; Li, J.; Park, M.; Zhang, Y.; Lui, G.; Chen, Z. Angew. Chem., Int. Ed. 2016, 55, 4977 –4982.

S39 Ma, T.; Ran, J.; Dai, S.; Jaroniec, M.; Qiao, S. Angew. Chem., Int. Ed. 2015, 54, 4646–4650.

S40 Su, C.; Cheng, H.; Li, W.; Liu, Z.; Li, N.; Hou, Z.; Bai, F.; Zhang, H.; Ma, T. Adv. Energy Mater. 2017, 7, 1602420.

S41 Mao, S.; Wen, Z.; Huang, T.; Hou, Y.; Chen, J. Energy Environ. Sci. 2014, 7, 609–616.

S42. Q. Hu, G. Li, G. Li, X. Liu, B. Zhu, X. Chai, Q. Zhang, J. Liu, and C. He, *Adv. Energy Mater.,* 2019, **9,** 1803867.

S43. T. Tam, S. Kang, M. Kim, S. Lee, S. Hur, J. Chung, and W. Cho, *Adv. Energy Mater.,* 2019, **9,** 1900945.

S44. Z. Yang, C. Zhao, Y. Qu, H. Zhou, F. Zhou, J. Wang, Y. Wu, and Y. Li, *Adv. Mater.,* 2019, **31,** 1808043.

S45. H. Han, Z. Bai, T. Zhang, X. Wang, X. Yang, X. Ma, Y. Zhang, L. Yang, J. Lu, *Nano Energy,* 2019, **56,** 724–732.

S46. J.Mahmood, F. Li, S. Jung, M. Okyay, I. Ahmad, S. Kim, N. Park, H. Jeong & J. Baek, *Nat. Nanotechnol.,* 2017, **12,** 441–446.

S47. J. Staszak-Jirkovský, C. Malliakas, P. Lopes, N Danilovic, S. Kota, K. Chang, B. Genorio, D. Strmcnik, V. Stamenkovic, M. Kanatzidis & N. Markovic, *Nature Mater.,* 2016, **15,** 197–203.

S48. Q. Lu, G. Hutchings, W. Yu, Y. Zhou, R. Forest, R. Tao, J. Rosen, B. Yonemoto, Z. Cao, H. Zheng, J. Xiao, F. Jiao, & J. Chen, *Nature Comm.,* 2015, **6,** 6567.

S49. Z. Yu, C. Lang, M. Gao, Y. Chen, Q. Fu, a Y. Duana and S. Yu, *Energy Environ. Sci.,* 2018, **11,** 1890-1897.

S50. Z. Ibupoto, A. Tahira, P. Tang, X. Liu, J. Morante, M. Fahlman, J. Arbiol, M. Vagin, A. Vomiero, *Adv. Funct. Mater.,* 2019, **29,** 1807562.

S51. K. Xu, H. Cheng, H. Lv, J. Wang, L. Liu, S. Liu, X. Wu, W. Chu, C. Wu, Y. Xie, *Adv. Mater.,* 2018, **30,** 1703322.

S52. Y. Huang, L. Hu, R. Liu, Y. Hu, T. Xiong, W. Qiu, M. Balogun, A. Pan, Y.Tong, *Appl. Catal. B: Environ.,* 2019, **251,** 181–194.

S53. Y. Zhu, H. Chen, C. Hsu, T. Lin, C. Chang, S. Chang, L. Tsai, and H. Chen, *ACS Energy Lett.,* 2019, **4,** 987−994.

S54. S. Jing a, L. Zhang a b, L. Luo b, J. Lu b, S. Yin b, P. Shen b, P. Tsiakaras, *Applied Catalysis B: Environmental,* 2018, **224,** 533–540.

S55. M. Zhang, J. Chen, H. Li, P. Cai, Y. Li, Z. Wen, *Nano Energy,* 2019, **61,** 576–583.

S56. Q. Fu, J. Dai, X. Huang, Y. Dai, Y. Pan, L. Yang, Z. Sun, T. Miao, M. Zhou, L. Zhao, W. Zhao, X. Han, J. Lu, H. Gao, X. Zhou, Y. Wang, Z. Ni, W. Ji, Y. Huang, *Adv. Mater.,* 2022, **34,** 2204247.

S57. A. Yang, K. Su, W. Lei, Y. Tang, X. Qiu, *Adv. Energy Mater.,* 2023, **13,** 2203150.

S58 G. Wang, J. Chang, S. Koul, A. Kushima, Y. Yang, J. Am. Chem. Soc. **143,** 11595−11601 (2021).

S59. D. Lyu, S. Yao, A. Ali, Z. Tian, P. Tsiakaras, P. Shen, Adv. Energy Mater. **11,** 2101249 (2021).

(S60) H. Zhang, M. Zhao, H. Liu, S. Shi, Z. Wang, B. Zhang, L. Song, J. Shang, Y. Yang, C. Ma, L. Zheng, Y. Han, W. Huang, Nano Lett. **21,** 2255−2264 (2021).

(S61) K. Cui, Q. Wang, Z. Bian, G. Wang, Y. Xu, Adv. Energy Mater. **11,** 2102062 (2021).

(S62) Liu, W.; Zhang, J.; Bai, Z.; Jiang, G.; Li, M.; Feng, K.; Yang, L.; Ding, Y.; Yu, T.; Chen, Z.; Yu, A. Adv. Funct. Mater. 2018, 28, 1706675.

(S63) Li, B.; Zhang, S.; Wang, B.; Xia, Z.; Tang, C.; Zhang, Q. Energy Environ. Sci. 2018, 11, 1723-1729.

(S64) Yang, T.; Venkatesan, S.; Lien, C.; Chang, J.; Zen, J. Electrochim. Acta, 2011, 56, 6205–6210.

(S65) Liu, Y.; Chen, S.; Quan, X.; Yu, H.; Zhao, H.; Zhang, Y.; Chen, G. J. Phys. Chem. C 2013, 117, 14992–14998.

(S66) Prabu, M.; Ketpang, K.; Shanmugam, S. Nanoscale, 2014, 6, 3173–3181.

(S67) Cao, R.; Thapa, R.; Kim, H.; Xu, X.; Kim, M.; Li, Q.; Park, N.; Liu, M.; Cho, J. Nat. Commun. 2013, 4, 2076.

(S68) Li, Y.; Gong, M.; Liang, Y.; Feng, J.; Kim, J.; Wang, H.; Hong, G.; Zhang, B.; Dai, H. Nat. Commun. 2013, 4, 1805.

(S69) Dhavale, V.; Kurungot, S. ACS Catal. 2015, 5, 1445–1452.

(S70) Lee, J.; Park, G.; Lee, H.; Kim, S.; Cao, R.; Liu, M.; Cho, J. Nano Lett. 2011, 11, 5362–5366.
(S71) An, L.; Li, Y.; Luo, M.; Yin, J.; Zhao, Y.; Xu, C.; Cheng, F.; Yang, Y.; Xi, P.; Guo, S. Adv. Funct. Mater. 2017, 27, 1703779.
(S72) Li, L.; Liu, C.; He, G.; Fan, D.; Manthiram, A. Energy Environ. Sci. 2015, 8, 3274–3282.
(S73) Lee, D.; Choi, J.; Feng, K.; Park, H.; Chen, Z. Adv. Energy Mater. 2014, 4, 1301389.
S74. Liu, X.; Park, M.; Kim, M.; Gupta, S.; Wu, G.; Cho, J. Angew. Chem., Int. Ed. 2015, 54, 9654–9658.
S75. Jung, J.; Risch, M.; Park, S.; Kim, M.; Nam, G.; Jeong, H.; Horn, Y.; Cho, J. Energy Environ. Sci. 2016, 9, 176–183.
S76. Wang, T.; Nam, G.; Jin, Y.; Wang, X.; Ren, P.; Kim, M.; Liang, J.; Wen, X.; Jang, H.; Han, J.; Huang, Y.; Li, Q.; Cho, J. Adv. Mater. 2018, 30, 1800757.
(S77) Fu, G.; Chen, Y.; Cui, Z.; Li, Y.; Zhou, W.; Xin, S.; Tang, Y.; Goodenough, J. Nano Lett. 2016, 16, 6516−6522.
(S78) Fu, G.; Cui, Z.; Chen, Y.; Li, Y.; Tang, Y.; Goodenough, J. Adv. Energy Mater. 2017, 7, 1601172.
(S79) Lee, D.; Fu, J.; Park, M.; Liu, H.; Kashkooli, A.; Chen, Z. Nano Lett. 2016, 16, 1794–1802.
(S80) Wang, J.; Wu, H.; Gao, D.; Miao, S.; Wang, G.; Bao, X. Nano Energy 2015, 13, 387–396.
(S81) Zhuang, X.; Gehrig, D.; Forler, N.; Liang, H.; Wagner, M.; Hansen, M.; Laquai, F.; Zhang, F.; Feng, X. Adv. Mater. 2015, 27, 3789–3796.
(S82) Li, C.; Han, X.; Cheng, F.; Hu, Y.; Chen, C.; Chen, J. Nat. Commun. 2015, 6, 7345.
(S83) Chen, Z.; Yu, A.; Higgins, D.; Li, H.; Wang, H.; Chen, Z. Nano Lett. 2012, 12, 1946–1952.
(S84) T. You and C. Hu, ACS Appl. Mater. Interfaces 2018, 10, 10064−10075.
(S85) P. Li, C. Hu, T. You, P. Chen, Carbon, 2017, 111, 813-821.
S86. M. Zhao, H. Liu, H. Zhang, W. Chen, H. Sun, Z. Wang, B. Zhang, L. Song, Y. Yang, C. Ma, Y. Han, W. Huang, Energy Environ. Sci., **14,** 6455–6463 (2021).
S87. N. Wagh, S. Shinde, C. Lee, J. Jung, D. Kim, S. Kim, C. Lin, S. Lee, J. Lee, Appl. Catal. B: Environ. **268**, 118746 (2020).

S88. Fu, J.; Hassan, F.; Li, J.; Lee, D.; Ghannoum, A.; Lui, G.; Hoque, M.; Chen, Z. Adv. Mater. 2016, 28, 6421–6428.

S89. Sumboja, A.; Lübke, M.; Wang, Y.; An, T.; Zong, Y.; Liu, Z. Adv. Energy Mater. 2017, 7, 1700927.

S90. Fu, J.; Zhang, J.; Song, X.; Zarrin, H.; Tian, X.; Qiao, J.; Rasen, L.; Lib, K.; Chen, Z. Energy Environ. Sci. 2016, 9, 663–670.

S91. Fu, J.; Lee, D.; Hassan, F.; Yang, L.; Bai, Z.; Park, M.; Chen, Z. Adv. Mater. 2015, 27, 5617–5622.

S92. T. Cui, Y. Wang, T. Ye, J. Wu, Z. Chen, J. Li, Y. Lei, D. Wang, Y. Li, *Angew. Chem. Int. Ed.,* 2022, **61,** e202115219.

S93. L. An, B. Huang, Y. Zhang, R. Wang, N. Zhang, T. Dai, P. Xi, C. Yan, *Angew. Chem. Int. Ed.,* 2019, **58,** 9459.

S94. C. Gu, X. Xie, Y. Liang, J. Li, H. Wang, K. Wang, J. Liu, M. Wang, Y. Zhang, M. Li, H. Kong, and C. Liu, *Energy Environ. Sci.,* 2021, **14,** 4451.

S95. Z. Pei, Z. Yuan, C. Wang, S. Zhao, J. Fei, L. Wei, J. Chen, C. Wang, R. Qi, Z. Liu, Y. Chen, *Angew. Chem. Int. Ed.,* 2020, **59,** 4793.

S96. C. Zhao, J. Liu, N. Yao, J. Wang, D. Ren, X. Chen, B. Li, Q. Zhang, *Angew. Chem. Int. Ed.,* 2021, **60,** 15281.

S97. Y. Zhang, H. Qin, M. Alfred, H. Ke, Y. Cai, Q. Wang, F. Huang, B. Liu, P. Lv, Q. Wei, *Energy Stor. Mater.,* 2021, **42,** 88-96.

S98. R. Chen, X. Xu, S. Peng, J. Chen, D. Yu, C. Xiao, Y. Li, Y. Chen, X. Hu, M. Liu, H. Yang, I. Wyman, and X. Wu, *ACS Sustain. Chem. Eng.,* 2020, **8,** 11501.

S99. G. Kresse and J. Hafner, *Phys. Rev. B*., 1993, **48**, 13115-13118.

S100. G. Kresse and J. Hafner, *Phys. Rev. B.*, 1994, **49**, 14251-14269.

S101. G. Kresse and J. Furthmuller, *Comp. Mater. Sci.*, 1996, **6**, 15-50.

S102. G. Kresse and J. Furthmuller, *Phys. Rev. B.*, 1996, **54**, 11169-11186.

S103. P. E. Blochl, *Phys. Rev. B*., 1994, **50**, 17953-17979.

S104. G. Kresse, D. Joubert, *Phys. Rev. B*., 1999, **59**, 1758.

S105. J. P. Perdew, K. Burke, *Phys. Rev. Lett*., 1996, **77**, 3865.

S106. S. Dudarev, G. Botten, S. Savrasov, C. Humphreys and A. Sutton, *Phys. Rev. B*., 1998, **57**, 1505-1509.

S107. H. Monkhorst, and J. Pack, *Phys. Rev. B*., 1976, **13**, 5188.

S108. G. Henkelman, A. Arnaldsson, H. Jonsson, *Comput. Mater. Sci.*, 2006, **36,** 354-360.